OXFORD

Journal of Petrology, 2023, **64**, 1–29
https://doi.org/10.1093/petrology/egad001
Advance access publication date 10 January 2023
Original Manuscript

Extreme Differentiation along Multiple Liquid Lines of Descent in Strongly Peralkaline Magma Series at Pantelleria (Italy)

John C White[1,*], Ray Macdonald[2,3], Bogusław Bagiński[2] and Katarzyna M Liszewska[4]

[1]Department of Physics, Geosciences, and Astronomy, Eastern Kentucky University, 521 Lancaster Ave., Science 3140, Richmond, KY 40475, USA
[2]Department of Geochemistry, Mineralogy and Petrology, Faculty of Geology, University of Warsaw al. Żwirki i Wigury 9302-089 Warsaw, Poland
[3]Environment Centre, Lancaster University, Lancaster LA1 4YQ, UK
[4]Institute of Geochemistry and Petrology, Department of Earth Sciences, ETH Zürich, Clausistrasse 25, 8092 Zürich, Switzerland

*Corresponding author: john.white@eku.edu, Tel: +1 859 622 1273

Abstract

The liquid line of descent from trachyte to pantellerite is controlled primarily by fractional crystallization of alkali feldspar, with whole-rock compositions following a fractionation path along the 'thermal valley' in the peralkaline haplogranite system Qz-Ab-Or-Ac-Ns and terminating at a minimum on the feldspar-quartz cotectic. Although whole-rock compositions for different pantelleritic suites follow nearly identical paths in a Qz-Ab-Or projection that terminate near the experimental minimum ($Qz_{40.5}Or_{34.5}Ab_{25}$ at 100 MPa, projected from Ac-Ns), matrix glass from samples with near-minimum compositions record extreme differentiation and form a 'cotectic delta' beyond the terminus of the 'thermal valley'. Although each glass trend shows a continuing increase in Zr to >3000 μg/g, the most evolved compositions in each suite differ in peralkalinity (mol [Na + K] / Al) and in the proportions of FeO^T, Qz, Ab, Or, and other components, which are related to subtle variations in the mafic phases controlled mainly by differences in oxygen fugacity (fO_2) and pressure (P). To determine the controls over mafic mineral crystallization in pantelleritic magmas and the various paths these suites take beyond the apparent (whole-rock) minimum, amphibole-phyric suites from the ~159 ka Cala dell'Altura and Cala Gadir volcanic centres and the ~8–10 ka Cuddia Mida volcanic centre on Pantelleria have been analyzed and compared with each other and with the well-characterized and amphibole-free, compositionally zoned Green Tuff, the ~46 ka caldera-forming ignimbrite of the Cinque Denti caldera. Differences between the extended fractionation trends may be ultimately attributed to variations in oxygen fugacity, depth of emplacement, and water saturation. Shallower (lower pressure) magma reservoirs such as the one for the Green Tuff are water-saturated and undergo degassing, which leads to an increase in relative oxygen fugacity. Deeper (higher pressure) magma reservoirs remain water-undersaturated and retain water in the melt, which both maintains lower relative oxygen fugacities and enables the crystallization of amphibole. Amphibole formation appears to require melt water contents >4 wt%, low oxygen fugacity (<ΔNNO-1.5), and low temperatures (<700°C), although fluorine may stabilize it at higher temperatures in some rocks.

Keywords: pantellerite, peralkaline, trachyte, oxygen fugacity, Extreme differentiation

INTRODUCTION

In Petrogeny's Residua System, as represented by the plane Qz-Ab-Or, felsic melts evolve towards and along a so-called 'thermal valley' towards a low-temperature point ('minimum') on the quartz-feldspar cotectic (Tuttle & Bowen, 1958). As Bailey & Schairer (1964) recognized, Qz-Ab-Or is not the residua system for peralkaline (*i.e.* peralkalinity index, P.I. [mol (Na + K) / Al] > 1.0) silicic magmas; continued feldspar fractionation drives them out of the plane towards increasing peralkalinity and into a system better represented by Qz-Or-Ab-Ac-Ns (where Ac is acmite [$NaFe^{3+}Si_2O_6$] and Ns is sodium metasilicate [$NaSiO_3$]), and terminating in a number of minima forming what might be termed a 'cotectic delta.' Attempts to describe these extended trends were made experimentally (Carmichael & MacKenzie, 1963; Bailey & Schairer, 1966; Thompson & MacKenzie, 1967) and by plotting compositional data into various projection schemes (Bailey & Macdonald, 1969; Roux & Varet, 1975). The form of the low-temperature zone within the alkali feldspar primary phase region in peralkaline silicic systems and the existence of a unique low-temperature point has remained, however, uncertain. For example, based on feldspar-rock relationships in peralkaline trachytes and rhyolites of the Menengai volcano, Kenya, Macdonald *et al.* (2011) suggested that several evolutionary paths are possible within the peralkaline low-temperature zone and that there is no unique endpoint.

Renewed interest in this question was raised by the discovery in peralkaline rhyolites of the Boseti volcano, Ethiopia, of very highly fractionated matrix glasses and melt inclusions in phenocrysts, with FeO^T (total Fe as Fe^{2+}) up to 17 wt%, Al_2O_3 as low as 2.3 wt% and SiO_2 ~65 wt% (Macdonald *et al.*, 2012). Highly fractionated glasses had previously been reported from pantellerites of Palo Alto, Terceira (Mungall & Martin, 1995), and in an obsidian from the Fantale volcano, Ethiopia (Lacroix, 1930). Macdonald *et al.* (2012) used the information set to suggest that the effective minimum composition (EMC) for peralkaline silicic magmas has ~5 wt% Al_2O_3, 13 wt% FeO^T and 66 ± 2 wt% SiO_2. The use of the

Received: May 2, 2022. **Revised:** December 28, 2022. **Accepted:** January 6, 2023

term 'effective' alluded to the fact that melts more evolved than this are unlikely to separate from their crystal mush hosts. The relatively high density due to the high Fe contents and their normal occurrence as low melt fractions is likely to inhibit crustal ascent and they remain trapped at depth. Possible exceptions are a pantellerite obsidian (lava?) from Fantale, Ethiopia (Lacroix, 1930) and a lava from Mt. Takahe, Marie Byrd Land, Antarctica (LeMasurier *et al.*, 2018). It is important to note that at Boseti the highly evolved compositions occur in pantellerites where alkali feldspar + fayalite + hedenbergite + oxide ± quartz is the dominant assemblage, whereas at Mt. Takahe alkali feldspar is the only reported phenocryst phase. In a majority of eruptive peralkaline silicic suites, the peralkaline varieties are derived by fractionation of metaluminous trachytic melts (White *et al.*, 2009; Neave *et al.*, 2012; Jeffery & Gertisser, 2018; Romano *et al.*, 2018; Brenna *et al.*, 2019; Macdonald *et al.*, 2021). Protracted fractionation of the peralkaline melts may result in Fe-rich, Al-depleted melts which represent the most evolved stages of peralkaline systems.

In this report, we provide mineral chemical and glass data for three peralkaline suites from the island of Pantelleria (adj. *Pantescan*) to give further insights into how the magmas evolved within the low-temperature zone. On Pantelleria several eruptive sequences include rocks spanning the compositional range from trachyte to pantellerite. Some contain glass (melt) with extreme compositions (up to 13.2 wt% FeO^T, as low as 4.7 wt% Al_2O_3, P.I. up to 3.5). Mineral and whole-rock chemical studies have revealed that each suite evolved along a different liquid-line-of-descent. This contribution focusses on the parameters (P, T, fO_2, H_2O_m) controlling the trends and the different assemblages formed. Particular attention is paid to the formation of amphibole which, in contrast to the other mafic phases such as olivine and pyroxene, shows considerable complexity in peralkaline silicic suites. For example, the composition of amphibole in comendites of the Olkaria complex, Kenya, changes with increasing whole-rock peralkalinity from kataphorite to richterite to silica-poor riebeckite (Marshall *et al.*, 2009). Macdonald *et al.* (2019) reported ferrorichterite in the Gold Flat pantelleritic ash flow tuff from southern Nevada. Ferrorichterite and arfvedsonite form small phenocrysts in pantellerites from the Eburru complex, Kenya (Ren *et al.*, 2006). On the island of Pantelleria, Italy, amphibole phenocrysts are uncommon and absent from most eruptive units. To date, they have been described only in rocks from three smaller volcanic centres (Fig. 1), namely those being used in this report to examine the nature of the low-temperature zone.

These suites are compared with the results of relevant experiments on comenditic and pantelleritic samples (Scaillet & Macdonald, 2001, 2003, 2006; Di Carlo *et al.*, 2010; Romano *et al.*, 2020) and the Green Tuff, the best-understood unit on the island (Williams, 2010; Williams *et al.*, 2014; Liszewska *et al.*, 2018; Romano *et al.*, 2019). The pantelleritic portion of the Green Tuff is compositionally similar to the suites studied here but, critically, does not contain amphibole phenocrysts, although it was produced in low temperature experimental runs on the Green Tuff even at moderate crystallinities, allowing us to look for differences in the crystallization conditions.

GEOLOGICAL SETTING

Pantelleria is located in the Strait of Sicily rift zone (SSRZ), a NW-SE trending transtensional rift system situated on the Pelagian Block, a northern promontory of the African plate (Catalano *et al.*, 2009; Fig. 1). The structure of the island is dominated by two nested calderas (Mahood & Hildreth, 1983, 1986): the La Vecchia caldera, dated at 140–146 ka by $^{40}Ar/^{39}Ar$ dating of feldspar (Rotolo *et al.*, 2013, 2021), and the Cinque Denti (or Monastero) caldera, formed at 45.7 ± 1 ka (2σ) (Scaillet *et al.*, 2013). The Cinque Denti caldera was created by the eruption of the compositionally zoned Green Tuff, which covered much of the island obfuscating the stratigraphy of the pre-caldera sequences. This was followed by a prolonged period of effusive activity from ~32–22 ka (Cornette *et al.*, 1983; Civetta *et al.*, 1984; Mahood & Hildreth, 1986; White *et al.*, 2022) that formed the trachytic Montagna Grande-Monte Gibele shield volcano, erupted from deeper levels in the Green Tuff reservoir (Ferla & Meli, 2006; Neave *et al.*, 2012), and several pantellerite shields and lava domes that erupted ~15–6 ka (Speranza *et al.*, 2010; Scaillet *et al.*, 2011) mostly from vents within the moat and along the rim of the caldera (Mahood & Hildreth, 1983, 1986; Civetta *et al.*, 1984, 1988; Rotolo *et al.*, 2007).

Pre-Green Tuff volcanic centres known to have erupted amphibole-phyric lavas and tuffs are limited to the Cala dell'Altura volcanic centre in Contrada Scirafi on the west coast and the Cala Gadir volcanic centre on the northeast coast. Gadir crops out along the coast as a volcanic shield buried by the Green Tuff and post-Green Tuff lavas; the Altura outcrop consists primarily of a sequence of welded and unwelded pumice fall deposits. Altura and Gadir occupy the same stratigraphic interval, situated below the 123 ka Cinque Denti Formation (based on $^{40}Ar/^{39}Ar$ dating of feldspar; Jordan *et al.*, 2018), which is consistent with the K-Ar age of 159 ± 8 ka for Altura reported by Mahood & Hildreth (1986). Amphibole microphenocrysts have been reported from the Cinque Denti Formation (formerly called Unit P), a crystal-rich, welded and rheomorphic ignimbrite dated at 123 ± 1.6 ka ($^{40}Ar/^{39}Ar$) by Rotolo *et al.* (2013); it is possible that the Altura, Cinque Denti Formation, and Gadir rocks are part of the same magmatic system, but this remains to be tested. Post-Green Tuff volcanic centres known to have erupted amphibole-phyric lavas are restricted to two proximal vents, Cuddia Mida (8.2 ± 2.2 ka K-Ar; Civetta *et al.*, 1984, 1988) and Serra della Fastuca (9.7 ± 0.6 ka $^{40}Ar/^{39}Ar$; Scaillet *et al.*, 2011), associated with the 'Hingeline Vent System' located within the Cinque Denti caldera on the north-western slope of Montagna Grande and are likely part of the same magma system (Mahood & Hildreth, 1986; Orsi *et al.*, 1989; Rotolo *et al.*, 2007).

Although these magma series are clearly not consanguineous, they demonstrate similar incompatible trace element ratios (*cf.* Jordan *et al.*, 2021). They have, for example, Zr/Nb (4.9–6.6) and chondrite-normalized La/Yb ratios (Fig. 2a; La_N/Yb_N 9.5–11.3; McDonough & Sun, 1995) that overlap with the Green Tuff (4.9–5.6 and 8.8–11.6, respectively; Liszewska *et al.*, 2018) and the low-Ti and P basalts on Pantelleria (3.3–5.9 and 8.3–10.8, respectively; White *et al.*, 2020). They also show nearly identical patterns on a multi-element variation diagram normalized to depleted MORB mantle [DMM] (Fig. 2b; Salters & Stracke, 2004) with patterns similar to that of a representative sample of basalt, having elevated concentrations for all elements except Ba, Sr, P, and Ti. The comparisons suggest that they were derived from a similar source and evolved along broadly similar compositional trends.

METHODS

Sixteen samples from amphibole-bearing units from the Cala dell'Altura ('Altura'), Cala Gadir ('Gadir'), and the Cuddia Mida / Serra della Fastuca ('Mida') volcanic centres were collected over the period 1998–2019 (Table 1). Data for four samples were presented in White *et al.* (2005, 2009), including two samples from Altura (98527 and 060522) that were erroneously identified as

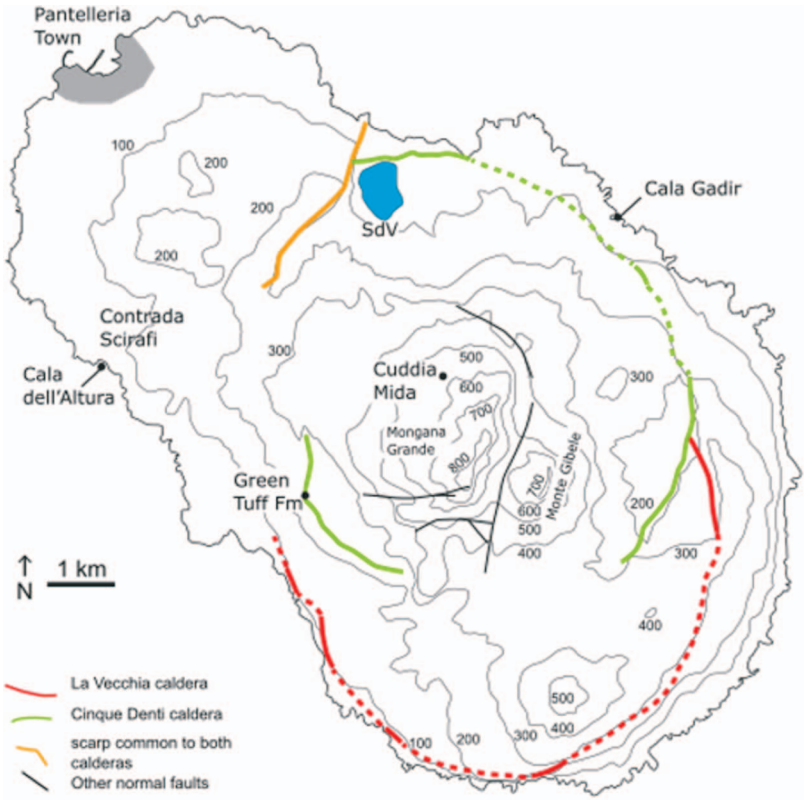

Eruptive Units	Age (ka)
Cuddia Mida / Serra della Fastuca	10 - 8
Montagna Grande Trachytes	32 - 22
Green Tuff Formation	46
Mordomo Formation	85
Acqua Formation	107
Cinque Denti Formation	123
Altura / Gadir Volcanic Centers	159 / >123
Arco Formation	175
Polacca Formation	186
Zinedi Formation	189

Bold, Italic: Units discussed in the text.
Italic: Units mentioned in the text.

Fig. 1. Map of Pantelleria showing topography (contour interval = 100 m), proposed calderas (after Mahood & Hildreth, 1986; Jordan *et al.*, 2018), post-caldera faults, the type locality of the Green Tuff (GT) Formation (Williams *et al.*, 2014), and the locations of Contrada Scirafi, Cala dell'Altura, Cala Gadir, and Cuddia Mida. SdV is Lago Specchio di Venere. Inset: Location of Pantelleria within the Strait of Sicily. Generalized stratigraphy of the eruptive units and the ages are adapted from Speranza *et al.* (2010), Scaillet *et al.* (2011, 2013), Rotolo *et al.* (2013, 2021); Jordan *et al.* (2018, 2021), and White *et al.* (2022).

Green Tuff by those authors (Nina Jordan, personal communication, 2016). Samples 090532 (Altura) and 090511–14 (Mida) were analysed at Activation Laboratories, Canada. Major elements and Ba, Be, Sc, Sr, V, Y, and Zr were analysed by ICP-OES on a fused bead (Code WRA-ICP-4B). Cu, Ni, Pb, S, and Zn were analysed by ICP-OES following acid digestion (Code 4B1). All other trace elements plus Cl were analysed by INAA (Codes 4B-INAA and 4F-Cl); F was determined with ion selective electrodes (Code 4F-F). Samples 060501–02 (Mida) and 190532 (Gadir) were also analysed at Activation Laboratories using ICP-OES for major elements and ICP-MS for trace elements (Code 4Lithoresearch). Samples 150531–33 were analysed at Bureau Veritas Commodities Canada Ltd. Major elements and Cr were analysed by ICP-OES, and trace elements, including REE, by ICP-MS. Loss on ignition (LOI) was determined by weight difference before and after ignition at 1000°C. Mean detection limits on major elements were 0.01 wt%, and between 0.10 and 10 μg/g for trace elements. Also included in our whole-rock dataset are WD-XRF analyses of three samples from Jordan (2014), used with permission: 171010–1 is a sample of Altura pantellerite sampled from the middle of the upper welded pyroclastic unit; Unk34A and Unk34B are samples of Gadir lava collected by Rebecca Williams.

New mineral and glass compositions (samples 090511–14, 150531–33, 190532) were determined by electron microprobe at the Inter-Institute Analytical Complex at the Department of Geochemistry, Mineralogy and Petrology, University of Warsaw, using a Cameca SX-100 microprobe equipped with four wavelength dispersive spectrometers. Minerals and glasses were analysed with a 15 kV accelerating voltage and 40 nA beam current, beam diameter from 5 to 20 μm, with counting times of 20 s

Table 1: Volcanic centres, sample locations, and phenocryst assemblages

		Location				Cpx				Aen	Amph		Ap		
Centre	Sample	Lat (N)	Long (E)	Matrix	Kfs	X-Fe_{tot}	apfu Na	Ol	FeTiOx	Ti#	X-Fe_{tot}	apfu Na(B)	Qtz	wt% F	Po
Altura	060522	36.79000	11.94611	Glass	Or23–31	0.63–0.67	0.06	Fa84	Mgt	–	–	–	–	–	+
	98527	36.79000	11.94611	Glass	Or38	0.84–0.89	0.18	–	Ilm	0.16	0.75–0.83	0.94	+	–	–
	060521	36.79000	11.94611	Pumice	Or36	+	+	–	+	+	+	+	+	–	–
	090532	36.78942	11.94622	Glass	+	+	+	–	+	+	+	+	+	–	–
	150532	36.78847	11.94678	Glass	Or36	0.87	0.18	–	Ilm	0.17	0.73–0.82	0.88–0.94	+	+	+
	150533	36.78860	11.94666	Glass	Or37	0.82–0.87	0.13–0.20	–	Ilm	0.17	0.69–0.82	0.83–0.91	+	+	+
	150531	36.78847	11.94678	Pumice	+	+	+	–	–	+	+	+	–	–	–
Gadir	190532	36.81061	12.02731	Glass	Or34–37	0.87–0.90	0.16–0.22	–	Ilm	0.17	0.75–0.80	0.92–1.00	+	2.83	–
Mida	090512	36.78694	11.99506	Glass	Or37	0.92–0.95	0.15–0.22	Fa98	Ilm	0.17	+	+	+	2.12	+
	090511	36.78539	11.99389	Glass	Or32–36	0.94–0.95	0.20–0.23	–	Ilm	0.16	+	+	+	–	+
	060501	36.78250	11.98639	Glass	Or34–37	0.94–0.95	0.23	Fa95	Ilm	0.16	0.91–0.92	1.13	+	+	+
	090514	36.78269	11.98647	Glass	Or13–37	0.94–0.95	0.15–0.30	–	+	0.16	0.93	1.11	+	2.44	–
	090513	36.78353	11.98822	Glass	+	+	+	–	Mgt	+	0.93–0.94	1.20	+	2.21	–
	060502	36.78167	11.98750	Glass	Or38–44	0.94–0.96	0.21	–	–	0.15	0.92–0.94	1.18	+	3.61	–

Kfs, Alkali Feldspar; Cpx, Clinopyroxene (apfu = atoms per formula unit); Ol, Olivine; FeTiOx, Iron-Titanium Oxide(s); Aen, Aenigmatite (Ti# = Ti / [Ti + Fe^T]); Amph, Amphibole (Na(B) = octahedral Na); Qtz, Quartz; Ap, Apatite; Po, Pyrrhotite. (+), observed but not analyzed; (–), not observed. X-Fe_{tot} = mol Fe^T/(Fe^T + Mg). Geodetic datum: WGS84. Descriptions of 060522, 98527, 060521, 060501, and 060502 adapted from White *et al.* (2005, 2009).

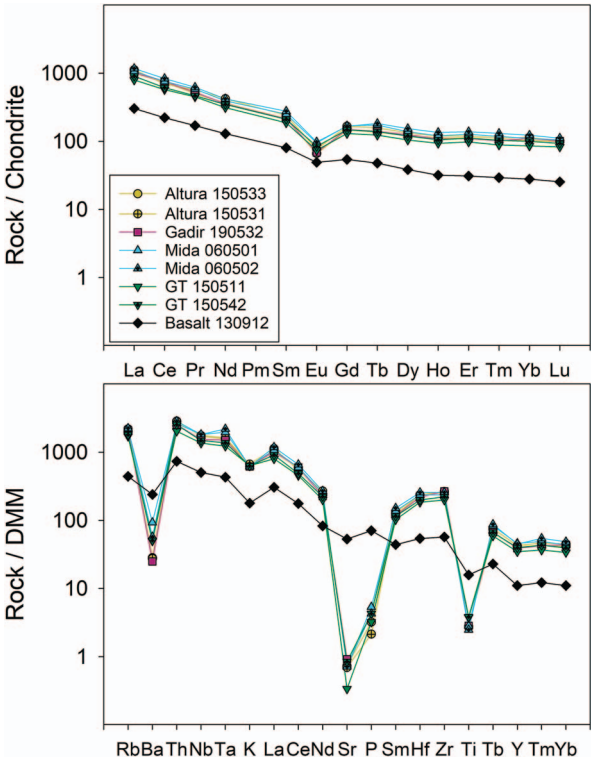

Fig. 2. Representative samples from each suite plotted on (a) a rare-earth element diagram (normalized to CI Chondrite; McDonough & Sun, 1995) and (b) a multi-element variation diagram (normalized to depleted MORB mantle [DMM]; Salters & Stracke, 2004). Included in each plot are representative samples of GT (Liszewska *et al.*, 2018) and a sample of low Ti-P basalt (130 912; White *et al.*, 2020) for comparison.

on peak and 10 s on each of two background positions. The standards, crystals, X-ray lines used, and generalized detection limits are given in Supplementary Table 1. The 'PAP' $\varphi(\rho Z)$ program (Pouchou & Pichoir, 1991) was used for corrections. Apatite was analysed using the technique outlined in Macdonald *et al.* (2008a).

White *et al.* (2005, 2009) presented only representative analyses of minerals from four samples used in this study; the previously unpublished complete datasets of electron microprobe analyses are included in our supplementary tables and figures; the analytical methods for these are described in those papers.

RESULTS

Petrography

The petrography of the new analysed samples is here described in some detail, since this is the first detailed account of the amphibole-phyric rocks on Pantelleria and since the textural relationships provide important constraints on interpreting the pre-eruptive crystallization conditions. A summary of the petrography and mineral chemistry is presented in Table 1. Salient points to note at this stage are: (i) While the dominant phenocrysts are the same, there are small differences, *e.g.* the occasional presence of olivine and/or magnetite only in the Mida samples. (ii) Evidence from mutual inclusion relationships (Fig. 3) suggests that the phenocryst phases generally crystallized together, in some cases in the first 10% modally. (iii) The mafic phases occur in variable proportions but generally amphibole > aenigmatite > clinopyroxene. (iv) Quartz occurs as a macrophenocryst in these amphibole-bearing rocks as opposed to the amphibole-free Green Tuff, in which it is absent except as heavily embayed microphenocrysts in the most evolved samples (Liszewska *et al.*, 2018; Romano *et al.*, 2019).

Cala dell'Altura volcanic centre

Sample 060522 is a crystal-rich (20–25 vol%) unwelded tuff with a partially devitrified pumiceous groundmass from the upper part of the Altura section. The phenocryst assemblage in 060522 is dominated (~20 vol%) by seriate inequigranular (2–10 mm) *anorthoclase*, with small amounts of olivine, augite, and magnetite. Samples 150532 and 150533 are gray-green, densely welded eutaxitic lapilli tuffs; 150532 was sampled from the welded unit above the unwelded pumice fall unit (150531) and 150533 was sampled from the welded unit below the pumice.

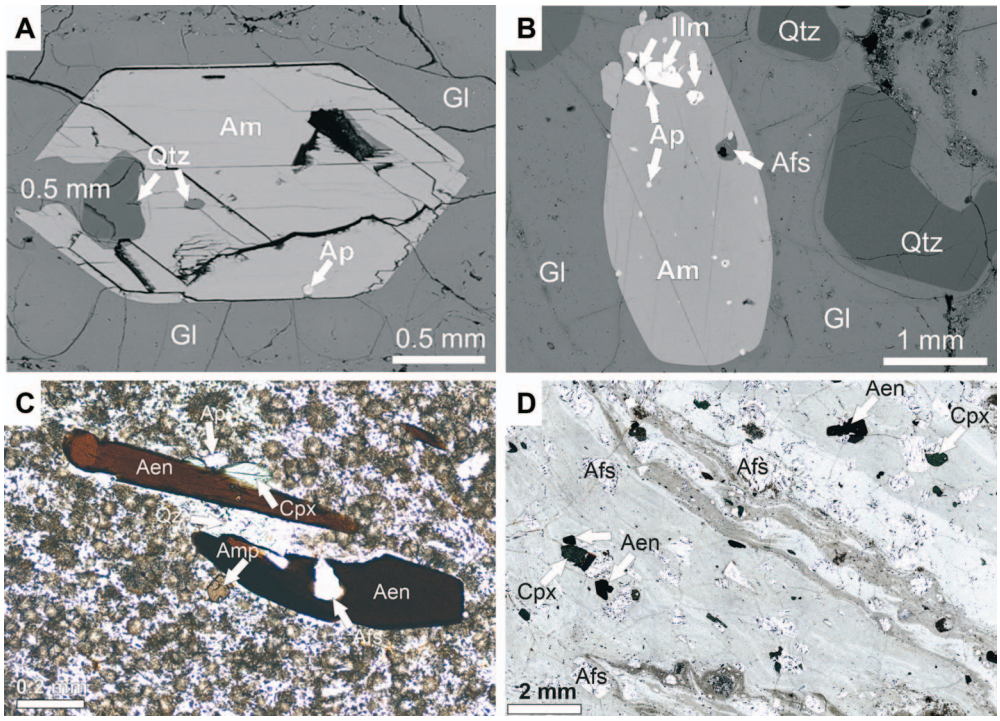

Fig. 3. (a) BSE image of sample 150532 (Altura) showing euhedral amphibole (Am) phenocryst with inclusions of quartz (Qtz) and apatite (Ap) in glass (Gl) matrix. (b) BSE image of sample 15033 (Altura) showing subhedral amphibole phenocryst with alkali feldspar (Afs), ilmenite (Ilm) and apatite inclusions. Note the partially resorbed, initially euhedral quartz. (c) Photomicrograph of sample 150531 (Altura) showing phenocrysts of aenigmatite (aen), clinopyroxene (cpx), and amphibole (amp). (d) Photomicrography of sample 090511 (Mida) showing streaky admixture of three glass types with phenocrysts of aenigmatite, clinopyroxene, and alkali feldspar.

The fiamme are strongly flattened and comprise layers of colourless glass and largely devitrified brown material. Sample 150531 is a creamy brown pumice tuff, consisting of a mixture of flattened pumice lapilli and glassy, partially devitrified zones. The phenocryst assemblage, 10–15 vol%, is alkali feldspar + aenigmatite + amphibole ± clinopyroxene ± quartz ± ilmenite ± apatite (Table 1; Fig. 3c). Most abundant is *anorthoclase,* forming in 150532 and 150533 clear, subhedral to euhedral crystals up to ~1 mm across. In 150531, the feldspars, up to 2 mm across, are commonly fractured. Zonation within crystals is very small (<Or_2). Contents of Fe_2O_3 are low (<1.5 wt%). Amphibole (fluorian ferrorichterite) is the most abundant mafic phase, forming prisms up to 2 mm long, pleochroic from chestnut brown to deep brown (Fig. 3). Aenigmatite occurs as elongated plates up to 1 mm long with prismatic terminations. The *clinopyroxene* phenocrysts in 150532 and 150533 are green, prismatic, and up to 900 μm in size. Quartz varies from hexagonal prims to rounded, partly embayed crystals up to 1.5 mm across. In 150531 it forms rare microphenocrysts. Occasional graphic intergrowths are found. Although quartz in Pantescan pantellerites has been considered to be a late-crystallizing phase, perhaps even formed during magma ascent (Di Carlo *et al.*, 2010), it is clearly intratelluric in the Altura rocks. It forms, for example, inclusions in amphibole phenocrysts in 150532 and is of comparable size to amphibole in 150533. Ilmenite (Ilm_{97}) is present as inclusions in hedenbergite and, less commonly, in amphibole. Fluorapatite forms prisms and subhedral plates, invariably associated with the mafic minerals. Pyrrhotite occurs as rare, small grains. Mutual inclusion relationships, *e.g.* ilmenite in amphibole (150533), amphibole in alkali feldspar (150532) and aenigmatite in alkali feldspar (150532), indicate that the phenocryst assemblage was forming in, or close to, equilibrium conditions.

Cala Gadir volcanic centre

Sample 190532 contains the phenocryst assemblage alkali feldspar-quartz-clinopyroxene- aenigmatite-ilmenite (<10 modal %). The quartz is unusually large, comparable to the largest feldspars. Clinopyroxene including ilmenite is intergrown in one case with feldspar. Amphibole forms euhedral cross-sections and prisms up to 600 x 400 μm in size.

Cuddia Mida volcanic centre

All samples from Mida belong to the 'hyalopantelleritic explosion breccia' unit of Rotolo *et al.* (2007). Samples 090511 and 090512 show a streaky admixture of glasses varying from colorless to pale grey to brown (Fig. 3d). Samples 090513 and 090514 are obsidians with pale homogeneous glass. All have the phenocryst assemblage (~10% modal) alkali feldspar + amphibole + aenigmatite + clinopyroxene + FeTi oxides + fluorapatite + quartz ± olivine. The feldspar varies from euhedral plates up to 700 μm long to small anhedra; some internal resorption is common; certain crystals in 090512 contain rounded melt inclusions. Aenigmatite forms thin rods and plates up to 0.5 mm across, with prismatic terminations. The amphibole, deep brown in color, also forms prisms, up to 0.6 mm long. Magnetite and ilmenite normally form small (~50 μm) equant crystals. Deep green clinopyroxene is less abundant than amphibole and aenigmatite and ranges from prismatic crystals up to 300 μm long to small ragged anhedra. Apatite is scarce, always associated with the mafic phases. Olivine has been positively identified only in sample 090512, forming

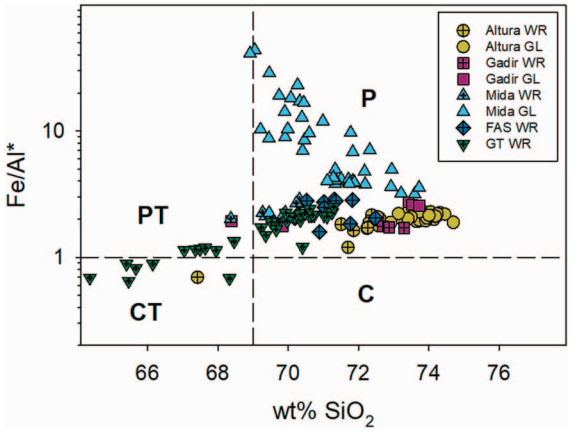

Fig. 4. Classification of silicic peralkaline (P.I. > 1.0) rocks following Le Maitre (2002) and Macdonald (1974), with $Fe/Al^* = 1.33 \cdot FeO^T / (Al_2O_3 - 4.4)$: CT, comenditic trachyte; C, comendite; PT, pantelleritic trachyte; P, pantellerite. WR, whole rock; GL, glass. Fastuca WR are WR analyses of the Serra della Fastuca pumice from Rotolo *et al.* (2007) and White *et al.* (2009). GT WR data are from Williams *et al.* (2014) and Liszewska *et al.* (2018).

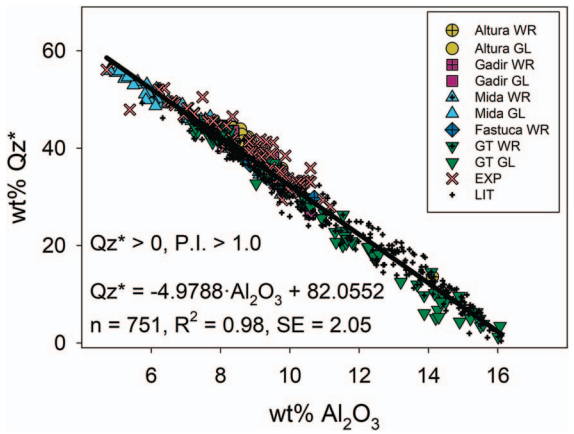

Fig. 5. Wt% Al_2O_3 plotted versus wt% Qz* for WR and GL samples from this study plus GT WR and glass analyses (Williams, 2010; Liszewska *et al.*, 2018; Romano *et al.*, 2019), WR analyses of Serra della Fastuca samples (Rotolo *et al.*, 2007; White *et al.*, 2009), experimental glasses (EXP; Di Carlo *et al.*, 2010 ; Romano *et al.*, 2020), and all other pantellerite WR analyses from Pantelleria (LIT; Civetta *et al.*, 1984, 1998; Mahood & Stimac, 1990; Kovalenko *et al.*, 1994; Prosperini *et al.*, 2000; Avanzinelli *et al.*, 2004; White *et al.*, 2005, 2009; Ferla & Meli, 2006; Parker & White, 2008; Jordan *et al.*, 2021).

small anhedral platelets. Quartz phenocrysts, up to 700 microns across, are usually partly resorbed and may contain feldspars.

Whole-rock and glass compositions

Whole-rock analyses are presented in Table 2. Representative matrix glass analyses are presented in Table 3 and the complete data set is presented in Supplementary Table 2. Samples are classified using the methods of Le Maitre (2002) and Macdonald (1974); nearly all are pantellerites (*viz.*, rhyolites [$SiO_2 > 69$ wt%], peralkaline [P.I. > 1.0], and pantelleritic [$Fe/Al^* = 1.33 \cdot FeO^T/(Al_2O_3 - 4.4) > 1.0$]; Fig. 4). In silica-oversaturated peralkaline rocks, due to crystallization of alkali feldspar normative Qz will increase relative to Ab and Or. Here we employ the term Qz* [$= Qz_n / (Qz_n + Or_n + Ab_n)$, where Qz_n, Or_n, and Ab_n are the CIPW normative components reported in wt%] as a differentiation index (*cf.* Blundy & Cashman, 2008; Wilke *et al.*, 2017; Jordan *et al.*, 2021). CIPW norms were calculated using the method of Kelsey (1965) with iron oxides adjusted following Le Maitre (1976; $FeO/FeO^T = 0.87 \pm 0.02$). For all the peralkaline analyses presented in this study plus all published analyses from the literature for both natural and experimental glasses for Pantelleria (n = 751) there is a strong negative correlation ($R^2 = 0.98$) between alumina (normalized anhydrous with total iron recalculated as FeO^T) and Qz* (Fig. 5). This observation enables us to slightly modify the Macdonald (1974) classification diagram for peralkaline rocks, allowing a more direct comparison between it and projections in Qz-Or-Ab-Ac-Ns for peralkaline compositions (Fig. 6). Compositional variations between Qz* and selected components are presented in Fig. 7.

Green tuff

The Green Tuff whole-rock analyses define a liquid line of descent (LLOD) confined within the 'thermal valley' of Carmichael & MacKenzie (1963) for peralkaline silicic melts. This LLOD extends from comenditic trachyte (63.9 wt% SiO_2; 5.8 wt% FeO^T) that plots near the feldspar join (1.27 wt% Qz*) to pantellerite (71.3 wt% SiO_2; 8.3 wt% FeO^T) that terminates at 39.0 wt% Qz*, near the Carmichael & MacKenzie (1963) experimental minimum of 40.5 wt% Qz*, at approximately constant values of Or (35.1 ± 1.5 wt%). These changes are accompanied by increases in P.I. (~1.0 to 1.8), Cl (~0.1 to 0.8 ± 0.2 wt%), and Zr (291 to 2060 μg/g) with decreases in TiO_2 (~0.8 to 0.5 wt%) and CaO (~1.2 to 0.4 wt%). A regression through the Green Tuff whole-rock data suggests that at $Qz_{40.5}$ values would be P.I. = 1.68 ± 0.1; 0.49 ± 0.05 wt% TiO_2; 71.69 ± 0.44 wt% SiO_2; 0.32 ± 0.08 wt% CaO; 1986 ± 102 μg/g Zr; 8.34 ± 0.38 wt% FeO^T; and 8.23 ± 0.23 wt% Al_2O_3. These values are plotted in Fig. 7 to serve as a reference point for comparison with the other suites; the regression parameters are in Supplementary Table 3. Previous workers have modelled this LLOD as the result of ~85–90% fractional crystallization of an assemblage dominated by anorthoclase (>90% of the fractionating assemblage) with subordinate augite, olivine, ilmenite, and apatite (Liszewska *et al.*, 2018; Romano *et al.*, 2019). The majority (n = 112) of published Green Tuff glasses and melt inclusions more evolved than this (*viz.*, Qz* > 39 wt%) have a nearly constant composition of $Qz_{42.8 \pm 1.3}Or_{36.6 \pm 1.7}Ab_{20.4 \pm 1.7}$, with 71.9 ± 0.1 wt% SiO_2, 8.2 ± 0.5 wt% FeO^T, 0.9 ± 0.2 wt% Cl, and P.I. = 1.9 ± 0.1, although Zr continues to increase from ~2000 to 3183 μg/g (Liszewska *et al.*, 2018; Romano *et al.*, 2019). The exceptions are matrix glass analyses from the precursor air-fall deposit of the Green Tuff (sample 150542; Liszewska *et al.*, 2018) that overlap with the Altura glass trend discussed below, which forms a 'horizontal trend' towards lower Or (to 23) at fairly constant Qz* (44.1 ± 0.4 wt%) along the feldspar-quartz cotectic, accompanied by decreases in P.I. (to 1.6), FeO^T (to 7.4 wt%), TiO_2 (to 0.4 wt%), and Cl (to 0.2 wt%) along with slight increases in SiO_2 (to 73.5 wt%) and Zr (to 2318 μg/g). Liszewska *et al.* (2018) attributed this trend to co-fractionation of aenigmatite with quartz on the cotectic.

Altura

Whole-rock compositions overlap with the Green Tuff in the 'thermal valley' in the Qz-Or-Ab projection from 13.6 to 40.6 wt% Qz* at nearly constant Or (33.8 ± 2.2 wt%), but occupy different locations in FeO^T-Al_2O_3 space. Altura samples follow a trend that runs parallel to the Green Tuff, but with FeO^T concentrations ~1.5 wt% lower at a given value of Al_2O_3 and Qz*. The Altura suite is represented by a single sample of comenditic trachyte

Table 2: Whole-rock analyses of amphibole-bearing units from Pantelleria

Group:	Cala dell'Altura								Cala Gadir			Cuddia Mida					
Sample ID:	**060522**	**150531**	**060521**	**150533**	**171010-1**	**090532**	**150532**	**98 527**	**Unk34B**	**190532**	**Unk34A**	**090511**	**090512**	**060501**	**090514**	**060502**	**090513**
Class:	CT	P	P	P	P	P	P	P	P	P	P	P	P	P	P	P	P
SiO_2, wt%	66.43	68.51	66.33	71.35	69.48	72.56	71.35	72.04	70.86	71.37	71.88	67.46	68.64	68.58	69.78	69.95	70.35
TiO_2	0.53	0.37	0.34	0.37	0.36	0.37	0.36	0.38	0.39	0.38	0.38	0.46	0.45	0.38	0.33	0.33	0.33
Al_2O_3	13.83	9.25	8.35	9.20	8.93	9.13	8.88	8.68	9.25	9.24	9.34	9.52	9.32	8.95	8.37	8.29	8.18
$Fe_2O_3{}^T$	5.52	6.93	6.54	6.91	6.73	7.08	7.10	7.78	7.15	7.28	7.16	8.78	8.80	8.71	8.89	8.81	9.12
MnO	0.23	0.26	0.23	0.25	0.25	0.26	0.26	0.26	0.27	0.26	0.27	0.29	0.29	0.30	0.30	0.31	0.31
MgO	0.28	0.32	0.68	0.21	0.16	0.13	0.09	0.10	0.46	0.28	0.42	0.19	0.11	0.06	0.07	0.04	0.10
CaO	0.83	0.19	0.28	0.31	0.29	0.34	0.27	0.32	0.10	0.30	bdl	0.91	0.62	0.52	0.44	0.39	0.66
Na_2O	6.08	4.65	5.50	5.65	6.23	5.67	5.86	5.72	5.13	4.62	4.88	6.52	6.32	6.92	6.56	6.98	6.62
K_2O	4.71	4.84	4.46	4.48	4.38	4.42	4.51	4.23	4.32	4.46	4.43	4.49	4.40	4.53	4.33	4.46	4.36
P_2O_5	0.09	0.02	0.04	0.03	0.02	0.02	0.01	0.03	0.03	< 0.01	0.02	0.06	0.03	0.05	0.02	0.04	0.02
SO_3	n.a.	n.a.	0.09	n.a.	0.14	0.02	n.a.	n.a.	0.34	n.a.	bdl	0.05	0.04	0.03	0.04	0.04	0.04
F	0.08	0.10	0.18	n.a.	n.a.	0.23	0.25	n.a.	n.a.	n.a.	n.a.	0.20	0.17	0.23	0.23	0.25	0.24
Cl	0.06	n.a.	1.44	n.a.	0.97	0.61	n.a.	n.a.	n.a.	n.a.	n.a.	0.56	0.56	0.70	0.72	0.68	0.78
H_2O^+	n.a.	n.a.	n.a.	n.a.	n.a.	< 0.1	n.a.	n.a.	n.a.	0.70	n.a.	0.3	0.5	n.a.	0.1	n.a.	0.3
H_2O^-	n.a.	n.a.	n.a.	n.a.	n.a.	< 0.1	n.a.	n.a.	n.a.	0.70	n.a.	< 0.1	< 0.1	n.a.	< 0.1	n.a.	< 0.1
LOI	0.46	4.10	6.75	0.70	2.15	−0.19	0.80	n.a.	0.45	1.70	0.62	−0.33	−0.77	0.00	−1.14	0.00	−0.87
Sum	99.13	99.54	101.22	99.46	100.08	100.65	99.74	99.54	98.74	101.29	99.29	99.45	99.48	99.97	99.04	100.57	100.54
O=F, Cl	0.05	—	0.40	—	0.22	0.23	—	—	—	—	—	0.21	0.20	0.25	0.26	0.26	0.28
Total	99.08	99.54	100.82	99.46	99.86	100.41	99.74	99.54	98.74	101.29	99.29	99.24	99.28	99.71	98.78	100.31	100.26
P.I.	1.09	1.39	1.66	1.54	1.68	1.55	1.64	1.61	1.42	1.34	1.37	1.64	1.63	1.82	1.85	1.97	1.91
Qz*	13.06	35.28	37.36	37.38	37.51	38.62	38.78	40.09	37.47	37.59	38.04	29.76	32.45	33.89	38.22	38.54	39.22
Be, μg/g	4	7	11	11	n.a.	13	8	n.a.	n.a.	14	n.a.	12	12	11	14	12	14
Sc	5	2	4	2	< 1.1	2.86	2	4	2.9	2	3.6	2.05	2.04	3	1.51	2	1.64
V	< 5	n.a.	< 5	n.a.	<0.8	< 5	n.a.	5	0.2	< 5	2.3	< 5	< 5	< 5	< 5	< 5	< 5
Cr	< 20	n.a.	< 20	n.a.	<0.7	4.4	n.a.	< 20	< 0.7	< 20	< 0.7	4	20.7	< 20	13.8	< 20	5.6
Co	< 1	0.4	< 1	0.7	3.8	< 0.1	0.3	3	8.1	< 1	7.4	< 0.1	< 0.1	< 1	< 0.1	< 1	< 0.1
Ni	2	<20	2	<20	<0.7	3	<20	< 5	< 0.7	< 20	< 0.7	2	4	< 1	2	< 1	3
Cu	4	n.a.	3	n.a.	<0.6	2	n.a.	n.a.	2.3	< 10	2.4	5	6	7	5	6	6
Zn	172	n.a.	334	n.a.	380.1	403	n.a.	468	370	390	403	379	388	401	462	417	455
Ga	31	33.1	33	33.2	35.3	n.a.	31.1	35	33.3	35	32.8	n.a.	n.a.	38	n.a.	36	n.a.
Ge	1.5	n.a.	2	n.a.	n.a.	n.a.	n.a.	3.4	n.a.	2.3	n.a.	n.a.	n.a.	2.3	n.a.	2.2	n.a.
As	< 5	n.a.	8	n.a.	7.9	11	n.a.	8	n.a.	< 5	n.a.	9	7	9	10	9	12
Se	n.a.	n.a.	n.a.	n.a.	n.a.	8.5	n.a.	n.a.	n.a.	n.a.	n.a.	5.6	9.2	n.a.	5.8	n.a.	9.1
Br	n.a.	n.a.	n.a.	n.a.	n.a.	19.3	n.a.	n.a.	n.a.	n.a.	n.a.	18.6	18.5	n.a.	22.5	n.a.	23.6
Rb	90	174.6	177	194.1	214.1	190	190.8	201	182	187	169	170	190	192	200	198	200
Sr	44	6.8	13	7.2	8.0	7	3.7	6	25.0	9	12.2	12	9	7	8	7	12
Y	79.4	173.5	208.0	164	195.3	168	168.9	162.8	151	159	183	155	153	188.0	182	183.0	185
Zr	917	2105.2	1926	2028	2292.0	1928	2067.4	1910	2346	2117	2345	1771	1640	1876	1958	2045	1986
Nb	167	369.8	339	361.9	426.8	n.a.	366.3	369.0	431	322	430	n.a.	n.a.	384	n.a.	384	n.a.

(Continued)

Table 2: Continued

Group:	Cala dell'Altura								Cala Gadir			Cuddia Mida					
Sample ID:	**060522**	**150531**	**060521**	**150533**	**171010-1**	**090532**	**150532**	**98 527**	**Unk34B**	**190532**	**Unk34A**	**090511**	**090512**	**060501**	**090514**	**060502**	**090513**
Mo	3	n.a.	15	n.a.	18.3	17	n.a.	n.a.	5	4	3	14	17	13	15	13	15
Ag	2.3	n.a.	3.3	n.a.	n.a.	3.0	n.a.	n.a.	n.a.	6.2	n.a.	3.0	3.1	3.4	3.2	3.1	3.5
Cd	< 0.5	n.a.	< 0.5	n.a.	n.a.	0.9	n.a.	n.a.	n.a.	n.a.	n.a.	1.2	1.1	0.5	1.2	< 0.5	1.2
Sn	6	22	13	15	15.5	n.a.	17	n.a.	6	14	n.a.	n.a.	n.a.	14	n.a.	14	n.a.
Sb	< 0.2	n.a.	< 0.2	n.a.	n.a.	0.8	n.a.	n.a.	n.a.	0.2	n.a.	0.8	0.6	< 0.2	0.9	< 0.2	1.1
Cs	0.2	2	2.1	2.0	15.5	2.4	2.3	2.1	13.0	0.8	16.6	2	2.1	2.7	2.5	2.7	2.8
Ba	548	33	43	34	11.1	37	34	36	43.9	30	12.9	89	83	112	70	69	80
La	171	266.3	281	238	229.1	234	237.8	250.44	201.9	240	258.1	210	216	252	244	278	250
Ce	247	427.9	440	449.9	472.1	358	435.9	425.65	489.6	464	528.8	321	330	463	373	511	382
Pr	38.2	52.78	60.9	46.99	n.a.	n.a.	50.14	46.12	n.a.	48.9	n.a.	n.a.	n.a.	54.4	n.a.	57.7	n.a.
Nd	130.0	192.6	206	165.2	181.4	149	172.7	167.76	154.3	162	189.6	128	134	179	152	192	154
Sm	27.4	35.69	42.6	31.95	n.a.	26.5	32.76	33.32	n.a.	31.7	n.a.	25	26	37.1	29.4	40.9	29.6
Eu	4.38	4.29	5.38	3.71	n.a.	3.9	3.87	3.93	n.a.	3.83	n.a.	3.92	4.09	5.31	4.53	5.49	4.65
Gd	20.0	33.1	38.9	29.20	n.a.	n.a.	30.79	29.67	n.a.	29.8	n.a.	n.a.	n.a.	33.5	n.a.	33.2	n.a.
Tb	3.77	5.68	6.86	4.90	n.a.	4.3	5.33	5.66	n.a.	5.04	n.a.	3.8	3.2	6.24	4.3	6.58	4.6
Dy	19.7	32.86	38.5	29.70	n.a.	n.a.	31.64	31.09	n.a.	30.7	n.a.	n.a.	n.a.	34	n.a.	37.8	n.a.
Ho	3.52	6.55	7.44	6.14	n.a.	n.a.	6.39	6.05	n.a.	5.97	n.a.	n.a.	n.a.	6.62	n.a.	7.44	n.a.
Er	10.40	19.07	21.8	17.92	n.a.	n.a.	18.77	19.44	n.a.	17.5	n.a.	n.a.	n.a.	20.3	n.a.	22.1	n.a.
Tm	1.61	2.8	3.2	2.59	n.a.	n.a.	2.68	2.90	n.a.	2.55	n.a.	n.a.	n.a.	2.95	n.a.	3.27	n.a.
Yb	10.30	18.4	19.4	16.76	n.a.	16	17.92	16.99	n.a.	17.8	n.a.	14.1	14.7	17.8	16.9	19.8	17.1
Lu	1.44	2.54	2.76	2.47	n.a.	2.26	2.49	2.60	n.a.	2.52	n.a.	1.93	2.05	2.62	2.29	2.78	2.35
Hf	21.9	47.3	46.2	47.4	n.a.	45.8	47	46.52	n.a.	43.7	n.a.	39	40.4	47.3	45.9	51	47.4
Ta	13.0	22.4	24.7	21.7	n.a.	23.9	22.3	23.7	n.a.	20.8	n.a.	22.6	22.4	27.3	26.6	30.5	26.7
W	2.5	4.4	4.2	4.5	n.a.	< 1	4.5	n.a.	n.a.	3.7	n.a.	< 1	< 1	4.8	< 1	5.7	< 1
Tl	0.1	n.a.	0.13	n.a.	n.a.	n.a.	n.a.	n.a.	n.a.	0.15	n.a.	n.a.	n.a.	0.2	n.a.	0.26	n.a.
Pb	9	n.a.	16	n.a.	15.3	11	n.a.	n.a.	18	13	19	11	10	20	13	20	14
Bi	< 0.1	n.a.	0.4	n.a.	n.a.	< 2	n.a.	n.a.	n.a.	< 0.1	n.a.	< 2	< 2	0.3	< 2	0.4	< 2
Th	16.9	38.7	35.3	39.3	40.1	38.9	38.4	38.03	43.1	35.1	44.1	33.7	33.6	36.4	39.6	39.2	39.8
U	3.65	11.6	11.4	11.6	11.1	12	11.1	12.1	5.6	8	6.5	10.2	10.5	13.2	12.8	15.4	12.7
La_N/Yb_N	11.3	9.8	9.8	9.6	—	9.9	9.0	10.0	—	9.2	—	10.1	10.0	9.6	9.8	9.5	9.9
Zr/Nb	5.49	5.69	5.68	5.60	5.37	—	5.64	5.18	5.44	6.57	5.45	—	—	4.89	—	5.33	—

Samples 060522, 98 527, 060521, 060501, and 060501 were previously presented by White *et al.* (2009), except for Ag, Bi, Tl, W, Sb, Sn, and As. Samples 171 010–1, Unk34A, and Unk34B are WD-XRF analyses from Jordan (2014); Unk34A and Unk34B were collected by R. Williams. Class: CT, Comenditic Trachyte; P, Pantellerite (Macdonald, 1974; Le Maitre, 2002). $Fe_2O_3{}^T$, total iron reported as Fe_2O_3; LOI, Loss on Ignition; n.a., not analyzed; bdl, below detection limit; P.I. (Peralkalinity Index) = mol Na + K/Al; La_N/Yb_N, chondrite-normalized (McDonough & Sun, 1995) La/Yb ratios.
$Qz^* = 100 \bullet Qz_n/(Qz_n + Or_n + Ab_n)$, CIPW norm calculated following Kelsey (1965) with iron recalculated following Le Maitre (1976).

Table 3: Representative matrix glass analyses

Group:	Cala dell'Altura						Cala Gadir		Cuddia Mida									
Sample ID:	150532		150533		150531		190532		090512								090514	
Point:	#6	#11	#6	#1	#1	#11	13 / 1.	18 / 1.	79 / 1.	11 / 1.	20 / 1.	21 / 1.	83 / 1.	77 / 1.	95 / 1.	94 / 1.	16/1	8 / 1.
SiO_2, wt%	73.51	74.11	72.40	75.68	72.48	72.77	67.61	72.34	68.90	70.87	71.00	71.39	69.73	69.38	68.82	67.67	72.56	70.71
TiO_2	0.44	0.39	0.39	0.28	0.38	0.41	0.51	0.45	0.62	0.54	0.40	0.44	0.59	0.74	0.66	0.73	0.31	0.25
Al_2O_3	8.39	8.57	8.84	8.70	8.72	8.41	10.15	8.15	9.13	6.94	6.74	6.21	5.84	6.07	5.16	4.71	7.53	7.19
FeO^T	6.17	6.93	6.79	5.89	6.41	6.61	7.83	7.80	8.00	9.57	8.64	9.39	10.76	11.00	11.68	12.98	8.54	8.21
MnO	0.25	0.29	0.27	0.00	0.32	0.23	0.00	0.34	0.33	0.37	0.33	0.37	0.44	0.43	0.48	0.51	0.32	0.31
MgO	0.09	0.09	0.09	0.07	0.08	0.07	0.55	0.13	0.06	0.04	0.04	0.05	0.06	0.07	0.10	0.08	0.06	0.04
CaO	0.28	0.14	0.07	0.16	0.31	0.26	0.70	0.35	0.39	0.32	0.41	0.43	0.51	0.53	0.60	0.59	0.37	0.32
Na_2O	5.88	5.93	5.88	5.92	5.40	5.38	3.95	4.49	6.60	6.29	6.04	6.19	5.92	5.70	6.48	5.94	5.56	7.21
K_2O	4.40	4.54	4.99	3.60	4.22	3.84	5.51	4.44	5.15	4.39	4.76	4.89	4.94	4.46	4.67	4.76	4.24	4.33
P_2O_5	bdl	bdl	bdl	bdl	bdl	bdl	0.00	0.03	0.02	0.00	0.02	0.02	0.00	0.09	0.03	0.04	0.03	0.01
SO_3	0.04	bdl	0.03	bdl	0.03	0.05	0.01	0.04	0.10	0.09	0.07	0.08	0.03	0.12	0.07	0.07	0.06	0.00
ZrO_2	n.a.	n.a.	n.a.	n.a.	0.30	0.40	0.97	0.46	0.26	0.42	0.38	0.34	0.46	0.31	0.50	0.48	0.34	0.43
F	n.a.	n.a.	n.a.	n.a.	n.a.	n.a.	0.40	n.a.	0.43	0.10	0.23	0.35	0.23	0.26	0.40	0.36	0.10	n.a.
Cl	0.31	0.60	0.49	0.57	0.68	0.81	0.05	0.07	0.89	0.90	0.89	0.94	1.11	1.02	1.15	1.28	0.87	0.88
Sum	99.76	101.59	100.24	100.87	99.03	98.84	97.26	99.10	100.88	100.85	99.58	100.74	100.14	99.86	100.30	99.71	100.88	99.44
O=F, Cl	0.07	0.14	0.11	0.13	0.15	0.18	0.18	0.02	0.38	0.25	0.30	0.36	0.35	0.34	0.43	0.44	0.24	0.20
Total	99.69	101.45	100.13	100.74	98.88	98.66	97.08	99.08	100.50	100.61	99.28	100.38	99.79	99.52	99.87	99.27	100.63	99.24
P.I.	1.72	1.71	1.71	1.57	1.54	1.55	1.23	1.50	1.81	2.18	2.24	2.49	2.58	2.34	3.05	3.17	1.82	2.30
Qz*	43.52	42.51	39.86	44.31	41.34	43.31	29.04	43.58	33.90	46.74	48.43	51.11	51.40	50.17	54.27	56.17	45.92	45.45
CIPW Norm																		
Qz	34.58	33.38	31.32	36.43	33.15	34.71	22.84	37.04	25.17	32.83	34.62	35.32	33.90	33.40	33.78	33.54	34.22	32.48
Or	26.13	26.54	29.54	21.19	25.33	23.13	33.58	31.17	30.64	26.09	28.53	29.04	29.49	26.75	27.93	26.18	25.11	25.91
Ab	18.75	18.60	17.72	24.60	21.70	22.30	22.25	22.24	18.43	11.32	8.33	4.75	2.57	6.43	0.53	0.00	15.19	13.08
Ac	3.04	3.33	2.95	3.36	3.41	3.74	3.79	2.01	2.62	4.10	3.68	3.83	4.34	4.94	4.32	5.06	4.39	3.03
Nms	6.47	6.34	6.70	5.00	4.85	4.62	1.85	2.06	8.11	8.74	9.17	10.13	10.04	8.58	11.66	10.58	6.29	10.54
Di	1.24	0.61	0.31	0.70	1.39	1.17	3.13	0.14	1.64	1.41	1.73	1.76	2.27	1.81	2.50	2.38	1.48	1.38
Hy	8.95	10.48	10.72	8.19	9.44	9.54	11.56	5.20	12.16	14.49	13.12	14.29	16.26	16.45	17.96	20.08	12.67	13.08
Il	0.84	0.73	0.74	0.53	0.73	0.79	1.00	0.15	1.18	1.02	0.78	0.83	1.13	1.42	1.26	1.40	0.59	0.47
Ap	0.00	0.00	0.00	0.00	0.00	0.00	0.00	0.00	0.04	0.01	0.04	0.05	0.00	0.20	0.07	0.10	0.06	0.02

FeO^T, total iron reported as FeO; LOI, Loss on Ignition; n.a., not analyzed; bdl, below detection limit; P.I. (Peralkalinity Index) = mol Na + K/Al; $Qz^* = 100 \cdot Qz_n/(Qz_n + Or_n + Ab_n)$.
CIPW norm calculated following Kelsey (1965) with iron oxides adjusted following Le Maitre (1976).

(67.8 wt% SiO_2; 5.07 wt% FeO^T) and several pantellerites (71.7–73.1 wt% SiO_2; 6.1–7.1 wt% FeO^T), with systematically higher SiO_2 and lower P.I. (1.1–1.7) than those seen in the Green Tuff for a given value of Qz* over a similar range of Zr (917–2292 μg/g). Altura matrix glasses have a nearly constant composition of $Qz_{42.4\pm1.3}Or_{32.2\pm2.8}Ab_{25.4\pm2.1}$, with P.I. = 1.7 ± 0.1, 73.7 ± 0.5 wt% SiO_2, 6.6 ± 0.2 wt% FeO^T, 0.39 ± 0.04 TiO_2, and 0.22 ± 0.07 wt% CaO, although Zr continues to increase to 2961 μg/g. Cl compositions range from 0.81 to 0.25 wt% and are uncorrelated with any other component, suggesting that this variation may be due to Cl loss during degassing or devitrification.

Gadir

The three samples from the Gadir volcanic centre are compositionally similar to Altura (~73.1 wt% SiO_2; ~6.6 wt% FeO^T) and plot near the experimental minimum in the Qz-Or-Ab projection ($Qz_{38.1}Or_{33.3}Ab_{28.6}$). Considering that they occupy the same stratigraphic interval, albeit on different sides of the island, this suggests that there may be some petrogenetic relationship between the two suites. Glass in the Gadir dome is highly devitrified, which may account for its uniformly low Cl contents and should suggest some caution with this sample. Zr concentrations increase from ~2000 to 3500 μg/g.

Mida

Whole-rock samples from Mida plot along the 'thermal valley' projected on the Qz-Or-Ab plane, extending from 29.9 to 40.9 wt% Qz* at nearly constant Or (35.1 ± 1.5 wt%). The analyses are compositionally similar to the Green Tuff with respect to SiO_2 (69.0–70.4 wt%), Zr (1640–2550 μg/g), and CaO (0.40–0.93 wt%) but have slightly higher P.I. (1.2–2.0) and FeO^T (7.8–8.2 wt%), with lower TiO_2 (0.47–0.32 wt%) and Cl (0.67 ± 0.09 wt%) at a given value of Qz*. Glasses in Mida vary by sample. Glass compositions are fairly homogenous in sample 090514, with a composition of $Qz_{45.9\pm1.1}Or_{35.8\pm0.9}Ab_{18.6\pm0.9}$, 71.7 ± 0.5 wt% SiO_2, 8.5 ± 0.2 wt% FeO^T, P.I. = 2.3 ± 0.2, and 2505 ± 446 μg/g Zr. Glass compositions in sample 090512, however, demonstrate an extreme differentiation trend: Qz* increases from 45 to 56 wt% as Ab decreases to zero, P.I. increases from 2.0 to 3.5, Zr increases from ~2000 to 4000 μg/g, CaO and SiO_2 both reverse their whole-rock trends and increase to 0.6 wt% and decrease to 69 wt%, respectively, and with the increase in Qz*, Al_2O_3 decreases to 4.8 wt% and FeO^T increases to 13.2 wt%. The most extreme compositions observed are very similar to those recorded in extremely fractionated magmas at Boseti, Ethiopia, which may, as noted earlier, represent the effective compositional minimum (EMC) composition for peralkaline silicic rocks

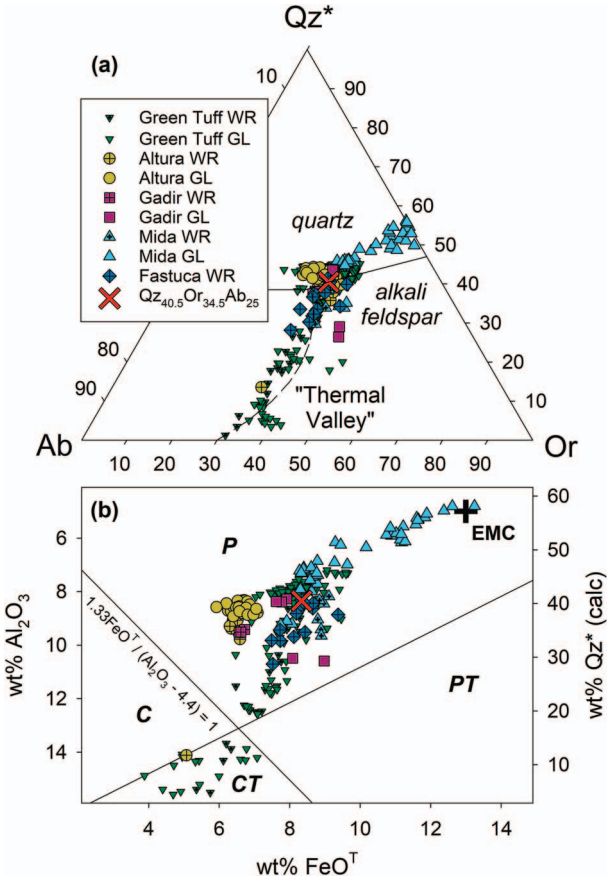

Fig. 6. (a) WR and matrix GL data for Altura, Gadir, Mida, Fastuca, and the GT plotted on an isobaric (100 MPa) projection from X (= H_2O + Na_2SiO_3 + $NaFeSi_2O_6$) of the alkali feldspar-quartz cotectic (solid line), location of the 'thermal valley' (dashed line), and ternary minimum (**X**) of the 8.3 wt% Ns + 8.3 wt% Ac plane in the peralkaline haplogranite system Q-Or-Ab-X following Carmichael & MacKenzie (1963). Serra della Fastuca analyses are from Rotolo *et al.* (2007) and White *et al.* (2009). GT WR data are from Williams *et al.* (2014) and Liszewska *et al.* (2018). Normative components were calculated following Kelsey (1965) with iron oxides distributed following Le Maitre (1976) (see Supplementary Table S2). (b) Modified Macdonald (1974) classification scheme for peralkaline rocks. P, Pantellerite; PT, Pantelleritic Trachyte; C, Comendite; CT, Comenditic Trachyte; EMC, Effective Minimum Composition (Macdonald *et al.*, 2012).

(Macdonald *et al.*, 2012). Cl in the glasses also shows a systematic increase from 0.8 to 1.3 wt as Qz* increases, possibly due to its higher solubility in more peralkaline and iron-rich melts (Webster *et al.*, 2015, 2020), the absence of a buffering exsolved vapor phase (*contra* Lowenstern, 1994), or both.

Mineral compositions

Feldspar

Representative feldspar analyses are presented in Table 4 and the complete data set is presented in Supplementary Table S4 and Fig. 8, which also includes analyses from the Green Tuff (Liszewska *et al.*, 2018). The total range is from *anorthoclase* (Or < 37 mol%) to *sanidine* (Or ≥ 37 mol%). Alkali feldspar compositions in all four suites are broadly similar. In the Green Tuff, alkali feldspars show a similarly continuous range of compositions with An decreasing from ~0.8 to 0.1 mol% as Or increases from ~20 to 35 mol%, after which it maintains a composition of 35.2 ± 1.0 mol% Or as An continues to decrease from 0.1 mol% to below the CaO detection limit (plotted as zero in Fig. 8b). Alkali feldspar in the sample of comenditic trachyte from Altura (060522) is compositionally zoned over a similar range from An_5Or_{22} to $An_{0.5}Or_{33}$, while alkali feldspars in the pantellerites have a nearly constant composition of <0.10 mol% An and 37.3 ± 1.1 mol% Or. Anorthoclase from the Gadir pantellerite is similar to the Green Tuff, with a nearly constant composition of An <0.25 mol% and 35.5 ± 1.3 mol% Or. Zonation within crystals is generally very small (< Or_{2-5}) and contents of Fe_2O_3 are low (<1.5 wt%). Although one sample from Mida (090514) has anorthoclase zoned from $An_{20}Or_{10}$ to An_5Or_{28}, most samples also have rather monotonous compositions of <0.20 mol% An and 37.2 ± 1.1 mol% Or. In the most extreme feldspars (≤0.01 mol% An), average Or compositions for the Green Tuff (35.2 ± 1.0 mol%) and Gadir (35.5 ± 1.5 mol%) are similar, Altura feldspars are similar but slightly higher (37.1 ± 1.1 mol%), and Mida are the highest (39.7 ± 2.2 mol%).

Arzilli *et al.* (2020) described a pressure- and H_2O-independent relationship between temperature and Or content in feldspar in peralkaline silicic melts, with compositions of >37 mol% Or (*i.e.* the anorthoclase-sanidine boundary) crystallizing at <720°C and compositions between 31–37 mol% Or crystallizing at ≥720°C. A comparison with our data suggests higher temperatures for the Green Tuff, lower temperatures for Mida, and intermediate temperatures for Altura and Gadir.

Clinopyroxene

Representative clinopyroxene analyses are presented in Table 5 and the complete data set in Supplementary Table S5 and Fig 9. Clinopyroxene analyses from the comenditic trachyte sample from Altura are similar to those from the comenditic trachyte section of the Green Tuff and classify as *augites* ($En_{19-21}Fs_{38-41}Wo_{39-41}$). Clinopyroxenes from the Altura and Gadir pantellerites have compositions similar to each other and to the most evolved samples from the Green Tuff ($En_{7-11}Fs_{50-56}Wo_{36-41}$) with all points but one classifying as *sodian augites* (Morimoto, 1988), and with Na increasing from 0.13 to 0.22 atoms per formula unit (apfu) as X-Fe_{tot} (= mol Fe^T / [Fe^T + Mg]) increases from 0.82 to 0.90. In contrast, clinopyroxenes from Mida are distinctly Fe- and Na-rich, classifying as sodian augites and *aegirine-augites* ($En_{3-4}Fs_{53-59}Wo_{39-43}$), with Na increasing from 0.11 to 0.30 apfu as X-Fe_{tot} increases from 0.92 to 0.95. Previous work (Larsen, 1976; Di Carlo *et al.*, 2010; Romano *et al.*, 2020) has shown that higher values of X-Fe_{tot} indicate both lower temperatures and lower relative oxygen fugacities.

Olivine

Representative olivine analyses are presented in Table 6 and the complete data set is presented in Supplementary Table 6. Olivine was not observed in the Gadir pantellerite and at Altura is found only as a phenocryst (Fa_{84}) in the comenditic trachyte. Unlike in other suites on Pantelleria such as the Green Tuff where it occurs in rocks with P.I. < 1.6 with compositions of Fa_{82-94} (Liszewska *et al.*, 2018; Romano *et al.*, 2020), olivine at Mida is found in rocks with a P.I. of up to ~1.8 and are classified as *fayalites* with a composition of Fa_{95-98}.

Aenigmatite

Representative *aenigmatite* analyses are presented in Table 7 and the complete data set in Supplementary Table S7. Aenigmatite is found in all samples except the Altura comenditic trachyte. Aenigmatites show very little variation with respect to X-Ti (= mol Ti/[Ti + Fe^T]), which has a nearly constant value of 0.17 ± 0.01 typical in peralkaline silicic rocks (Nicholls & Carmichael, 1969). However, there is a small amount (~2%) of the substitution $^{VIII}Ca^{2+}$

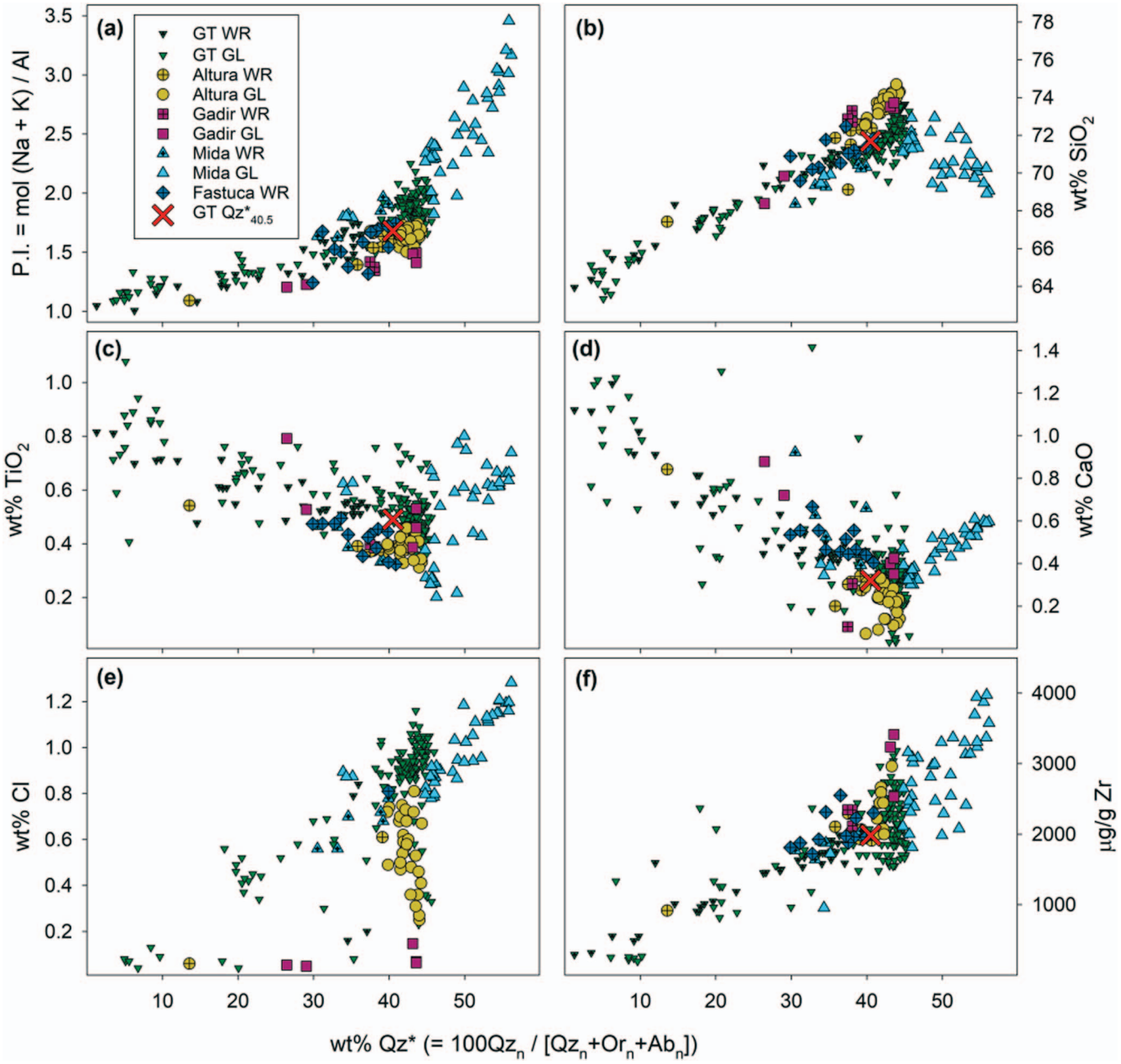

Fig. 7. Compositional variation diagrams that plot (a) P.I., (b) wt% SiO_2, (c) wt% TiO_2, (d) wt% CaO, (e) wt% Cl, and (d) μg/g Zr versus wt% Qz* (= 100·Qz_n / [$Qz_n + Ab_n + Or_n$]). GT data from Williams (2010), Liszewska *et al.* (2018) and Romano *et al.* (2019); Fastuca data are from Rotolo *et al.* (2007) and White *et al.* (2009). The red **X** symbol indicates the location of the projected intersection of the 'thermal valley' with the Carmichael & Mackenzie (1963) minimum on the alkali feldspar-quartz cotectic at Qz* = 40.5 (see Supplementary Table S3 for details.)

+ $^{VI}Al^{3+} = {}^{VIII}Na^{+} + {}^{IV}Si^{4+}$ within the individual series (Fig. 10), with aenigmatite from the Green Tuff generally being more calcic ($Ca^{2+} + Al^{3+} = 0.15–0.25$), which may have allowed it to stabilize at a slightly higher temperature and/or higher oxygen fugacity (Hodges & Barker, 1973; Larsen, 1977; Gaeta & Mottana, 1991).

Fe-Ti oxides

Representative oxide analyses are presented in Table 8 and the complete set of analyses in Supplementary Table S8. Oxides were observed in all but one sample from Altura and one from Mida and consist dominantly of *ilmenite*, although *magnetite* is the sole oxide in the Altura comenditic trachyte (Usp_{66}) and in a single sample from Mida (090513; Usp_{75}). Ilmenite ranges in composition from $Ilm_{95–98}$ at Altura, $Ilm_{96–97}$ at Gadir, and $Ilm_{96–99}$ at Mida, which all overlap with compositions in the Green Tuff ($Ilm_{95–98}$).

Amphibole

Representative amphibole analyses are presented in Table 9 and the complete data set in Supplementary Table S9 and Fig. 11. All amphiboles classify as *ferrorichterites* in the scheme of Hawthorne *et al.* (2012). Amphiboles from Altura and Gadir have similar compositions with respect to Fe and Na, but the Altura amphiboles have much higher fluorine concentrations (1.38–1.87 wt%; ~0.66–0.92 apfu) than Gadir (0.47–0.98 wt%; ~0.22–0.48 apfu) and Mida (0.47–0.57 wt%; ~0.24–0.29 apfu), although chlorine concentrations are similar in each series (0.05–0.07 wt%). As with the clinopyroxenes, amphiboles from Mida are higher in Na_B

Table 4: Representative alkali feldspar analyses

Group:	Cala dell'Altura					Gadir		Cuddia Mida								
Sample:	060522		150532	150533	98527	190532		090514		090511		090512	060501		060502	
Point:	#18	#67	21 /1.	2 / 4.	#8	40 / 10.	38 / 14.	7 / 1.	52 / 1 .	15 / 1.	5 / 1.	5 / 1.	#103	#19	#36	#38
Class:	Anr	Anr	Anr	Anr	San	Anr	Anr	Anr	Anr	Anr	Anr	San	Anr	San	San	San
SiO_2, wt%	66.41	65.72	67.38	67.41	67.89	67.61	67.91	64.19	67.90	67.86	67.50	66.03	65.47	66.75	66.41	65.74
Al_2O_3	20.49	18.99	17.51	17.88	18.40	18.58	18.43	21.16	17.45	18.42	17.43	17.19	19.70	18.00	18.50	18.05
FeO^T	bdl	bdl	1.04	0.95	0.87	0.79	0.78	0.30	0.93	0.23	1.32	1.00	0.36	1.08	0.86	1.14
CaO	0.92	0.09	bdl	bdl	0.00	0.04	0.01	3.64	0.004	0.50	0.01	0.02	0.39	0.01	0.01	0.00
Na_2O	8.20	7.51	7.40	7.39	7.00	7.67	7.29	7.82	7.26	7.17	7.12	7.05	7.16	7.16	7.16	6.17
K_2O	3.83	5.60	6.20	6.47	6.53	5.95	6.38	2.16	6.42	5.43	6.20	6.36	5.85	6.47	6.16	7.38
Total:	99.85	97.92	99.54	100.10	100.69	100.65	100.80	99.27	99.97	99.62	99.57	97.66	98.92	99.47	99.09	98.48
Formula (MT_4O_8)																
Si	2.94	2.99	3.03	3.02	3.02	3.00	3.01	2.866	3.04	3.02	3.03	3.03	2.96	3.01	3.00	3.00
Al	1.09	1.02	0.93	0.94	0.96	0.97	0.96	1.113	0.92	0.97	0.92	0.93	1.05	0.96	0.98	0.97
Fe^{3+}	0.00	0.00	0.04	0.04	0.03	0.03	0.03	0.011	0.03	0.01	0.05	0.04	0.01	0.04	0.04	0.04
$\sum T$	4.02	4.01	4.00	4.00	4.01	4.01	4.01	3.99	3.99	4.00	4.01	4.00	4.02	4.01	4.02	4.02
Ca	0.04	0.00	0.00	0.00	0.00	0.00	0.00	0.174	0.63	0.02	0.00	0.00	0.02	0.00	0.00	0.00
Na	0.71	0.66	0.65	0.64	0.60	0.66	0.63	0.677	0.37	0.62	0.62	0.63	0.63	0.63	0.60	0.55
K	0.22	0.32	0.36	0.37	0.37	0.34	0.36	0.123	0.00	0.31	0.36	0.37	0.34	0.37	0.36	0.43
ΣM	0.97	0.99	1.00	1.01	0.97	1.00	0.99	0.97	1.00	0.95	0.98	1.00	0.98	1.00	0.97	0.98
An, mol%	4.54	0.45	0.00	0.00	0.00	0.17	0.03	17.85	0.02	2.52	0.03	0.09	1.90	0.06	0.05	0.00
Ab	73.02	66.77	64.47	63.46	61.95	66.09	63.44	69.50	63.20	65.08	63.55	62.72	63.83	62.67	62.33	55.95
Or	22.45	32.78	35.53	36.54	38.04	33.74	36.53	12.65	36.79	32.40	36.42	37.19	34.27	37.27	37.62	44.05

Class: Anr, Anorthoclase; San, Sanidine. FeO^T, total iron reported as FeO. bdl, below detection limit. Components: An, Anorthite; Ab, Albite; Or, Orthoclase.

(1.11–1.20 apfu) and X-Fe_{tot} (0.93–0.94) than those at Altura and Gadir (0.70–1.03 apfu Na_B; X-Fe_{tot} = 0.69–0.82). A-site occupancy ($Na_A + K_A$) in the amphiboles is also lower in Altura and Gadir samples (0.80 ± 0.03) than in the Mida samples (0.88 ± 0.04) but does not correlate with X-Fe_{tot}. The higher F contents in the Altura and Gadir samples compared to Mida may have allowed amphibole to stabilize at higher temperatures in the suites (Ernst, 1962; Giesting & Filiberto, 2014), and the greater range in compositions may suggest that amphibole crystallized continuously over a wider compositional interval during melt differentiation in these suites, whereas it may have only crystallized during the last stages of differentiation prior to eruption at Mida.

Apatite

Representative analyses of *fluorapatite* are presented in Table 10 and the complete dataset in Supplementary Table S10. The sample from Gadir (190532) contains up to 8% britholite component, as determined by the substitution $\Sigma REE^{3+} + Si^{4+} = Ca^{2+} + P^{5+}$. Those from Mida and Altura have britholite components ranging between 1–7% and 5%, respectively. The analyses are similar to those reported from Pantelleria by Mahood & Stimac (1990) and Liszewska *et al.* (2018).

Summary

The phenocrysts in the Pantescan suites show compositional differences, some, at least, related to the degree of evolution of the host (as measured by wt% Qz*) and temperature. Mineral compositions imply low relative oxygen fugacities and lower temperatures (<720°C) for the amphibole-bearing suites compared to the Green Tuff. The next sections use petrographic, compositional, and mineral chemical data to describe quantitatively the evolutionary paths of the various suites.

DISCUSSION

Liquid lines of descent

Mineralogical controls on liquid lines of descent (LLOD) can be constrained by mass balance and trace element modelling. Like most models, mass balance methods do not provide unique solutions; therefore, we present only those calculations that resulted in the lowest possible sum of the squares of the residuals ($\Sigma r^2 << 1$) with predicted mineral assemblages consistent with observed petrography and melt fractions (F) similar to those approximated by incompatible trace element geochemistry ($F(Zr) = X(Zr)^{parent} / X(Zr)^{daughter}$, taking $D(Zr) \approx 0$). All calculations were performed with Microsoft Excel as described in White *et al.* (2009). Model results are summarized in Table 11 and detailed models are presented in Supplementary Table S11.

Green tuff ignimbrite

Four models are presented to provide a detailed description of the LLOD of the Green Tuff. The whole-rock trend that defines the 'thermal valley' is described in Model A1, which uses samples from the Green Tuff type section (Williams, 2010; Williams *et al.*, 2014) for the model parent (sample GT44F: 9.2 wt% Qz*, 487 μg/g Zr, P.I. = 1.15) and daughter (GT44B: 39.0 wt% Qz*, 2021 μg/g Zr, P.I. = 1.77). GT44F was sampled from 400 cm above the base of the section but was selected over higher samples because its lower crystal (<20 vol%) and Ba (<1500 μg/g) contents make it less likely to have been affected by feldspar accumulation (White *et al.*, 2009).

Table 5: Representative clinopyroxene analyses

Group:	Cala dell'Altura						Gadir		Cuddia Mida						
Sample:	060522	150532	150533		98527		190532		090511	090512		060501	090514	060502	
Point:	#85	30 / 1.	3 / 14.	3 / 1.	#8	#4	35 / 1.	37 / 6.	8 / 1.	28 / 1	60 / 1	#10	41 / 1	#29	#33
Class:	Aug	Na-Aug	Na-Aug	Na-Aug	Na-Aug	Ae-Aug	Na-Aug	Ae-Aug	Ae-Aug	Na-Aug	Ae-Aug	Na-Aug	Ae-Aug	Na-Aug	Ae-Aug
SiO_2, wt%	49.75	49.31	49.76	49.55	49.23	49.09	49.98	49.54	47.92	47.54	48.03	48.58	48.28	47.90	48.78
TiO_2	0.39	0.35	0.41	0.29	0.26	0.25	0.37	0.44	0.34	0.31	0.49	0.46	0.29	0.28	0.29
Al_2O_3	0.29	0.14	0.13	0.14	0.14	0.13	0.15	0.13	0.14	0.11	0.13	0.02	0.14	0.10	0.11
FeO^T	21.26	26.69	26.62	26.78	27.09	27.22	26.86	27.78	28.38	28.31	28.76	29.16	28.19	28.84	29.24
MnO	1.80	1.54	1.53	1.56	1.79	1.53	1.57	1.54	1.16	1.38	1.30	1.36	1.08	1.21	1.12
MgO	6.36	2.31	3.10	2.15	2.95	2.04	2.96	1.69	0.90	1.30	0.82	0.80	0.80	1.09	0.76
CaO	18.56	16.75	16.83	16.34	16.71	16.57	16.60	16.09	16.10	17.90	16.52	14.90	15.19	16.51	14.91
Na_2O	0.74	2.26	1.64	2.50	1.79	2.54	2.05	2.79	2.96	1.89	2.74	3.18	3.80	2.45	3.74
Sum	99.15	99.36	100.02	99.30	99.95	99.37	100.53	100.01	97.88	98.73	98.79	98.46	97.76	98.39	98.95
Recalculated FeO^T															
Fe_2O_3	1.99	5.60	3.31	5.79	5.28	7.20	4.91	7.00	8.74	7.33	8.37	8.13	10.90	7.79	10.64
FeO	19.48	21.65	23.64	21.57	22.34	20.74	22.44	21.48	20.51	21.72	21.23	21.85	18.38	21.83	19.67
Total	99.35	99.92	100.35	99.88	100.48	100.09	101.02	100.71	98.76	99.46	99.62	99.28	98.85	99.17	100.02
X-Fe_{tot}	0.65	0.87	0.83	0.87	0.84	0.88	0.83	0.90	0.95	0.92	0.95	0.95	0.95	0.94	0.96
Formula ($M2M1T_2O_6$)															
Si	1.980	1.990	1.998	1.998	1.979	1.979	1.991	1.987	1.969	1.950	1.962	1.986	1.971	1.966	1.973
^{IV}Al	0.014	0.007	0.002	0.002	0.006	0.006	0.007	0.006	0.007	0.005	0.006	0.001	0.007	0.005	0.005
$^{VI}Fe^{3+}$	0.006	0.004	0.000	0.000	0.015	0.015	0.002	0.007	0.025	0.045	0.032	0.013	0.022	0.029	0.022
ΣT	2.000	2.000	2.000	2.000	2.000	2.000	2.000	2.000	2.000	2.000	2.000	2.000	2.000	2.000	2.000
^{VI}Al	0.000	0.000	0.004	0.004	0.000	0.000	0.000	0.000	0.000	0.000	0.000	0.000	0.000	0.000	0.000
$^{VI}Fe^{3+}$	0.053	0.166	0.100	0.176	0.145	0.204	0.145	0.204	0.246	0.181	0.225	0.237	0.313	0.212	0.302
Ti	0.012	0.011	0.012	0.009	0.008	0.008	0.011	0.013	0.010	0.010	0.015	0.014	0.009	0.009	0.009
Mg	0.378	0.139	0.186	0.129	0.177	0.123	0.176	0.101	0.055	0.079	0.050	0.049	0.049	0.067	0.046
Fe^{2+}	0.557	0.684	0.697	0.682	0.670	0.666	0.668	0.681	0.689	0.730	0.710	0.699	0.627	0.713	0.643
Mn	0.000	0.000	0.000	0.000	0.000	0.000	0.000	0.000	0.000	0.000	0.000	0.000	0.003	0.000	0.000
ΣM1	1.000	1.000	1.000	1.000	1.000	1.000	1.000	1.000	1.000	1.000	1.000	1.000	1.000	1.000	1.000
Mg	0.000	0.000	0.000	0.000	0.000	0.000	0.000	0.000	0.000	0.000	0.000	0.000	0.000	0.000	0.000
Fe^{2+}	0.091	0.046	0.096	0.045	0.080	0.033	0.080	0.039	0.016	0.015	0.015	0.048	0.000	0.037	0.022
Mn	0.061	0.053	0.052	0.053	0.061	0.052	0.053	0.052	0.040	0.048	0.045	0.047	0.035	0.042	0.038
Ca	0.792	0.724	0.724	0.706	0.720	0.716	0.709	0.691	0.709	0.787	0.723	0.653	0.664	0.726	0.646
Na	0.057	0.177	0.128	0.195	0.139	0.199	0.159	0.217	0.235	0.150	0.217	0.252	0.301	0.195	0.293
ΣM2	1.000	1.000	1.000	1.000	1.000	1.000	1.000	1.000	1.000	1.000	1.000	1.000	1.000	1.000	1.000
X-En	0.2125	0.0884	0.1114	0.0844	0.1107	0.0824	0.1088	0.0676	0.0394	0.0549	0.0355	0.0338	0.0384	0.0461	0.0351
X-Fs	0.3647	0.4646	0.4765	0.4747	0.4702	0.4703	0.4632	0.4811	0.5060	0.5147	0.5146	0.5147	0.4959	0.5161	0.5105
X-Wo	0.4228	0.4470	0.4120	0.4409	0.4191	0.4473	0.4280	0.4513	0.4546	0.4305	0.4499	0.4516	0.4657	0.4378	0.4543

Class: Aug, Augite; Na-Aug, Sodian Augite; Ae-Aug, Aegirine-Augite. Iron oxides recalcualted following Papike *et al.* (1974). Formula: ΣT, sum of tetrahedral cations; ΣM1, sum of octahedral M1 site catiors; ΣM2, sum of octahedral M2 site cations. Components (Lindsley, 1983): Wo, Wollastonite; En, Enstatite; Fs, Ferrosilite; Wo, Wollastonite.

Model A2 also models crystal fractionation along the 'thermal valley' but uses a glass analysis from sample 150 544 (Liszewska *et al.*, 2018) with a composition most similar to the average value of highly evolved compositions ($Qz^* > 40.5$ wt%). Both models have excellent fits ($\Sigma r^2 = 0.003$ and 0.010, respectively) with similar results. As would be expected, the melt fraction for the glass daughter (A2) is lower (0.254) than that calculated for the whole rock (0.279). Fractionating assemblages are also similar, both dominated by alkali feldspar (0.64–0.67, or 88–89% of the fractionating assemblage) with subordinate clinopyroxene, olivine, aenigmatite, ilmenite, and apatite. Crystallization model (B) tests the origin of this same glass analysis (150544) from its whole-rock host (30.8 wt% Qz^*). This model has similarly good results ($\Sigma r^2 = 0.067$; $F = 0.733$) and predicted alkali feldspar fractions (0.22, or 88% of the fractionating assemblage) but requires a greater role for aenigmatite (0.03), a smaller amount of clinopyroxene (0.01), and no olivine. Mass balance models for the LLOD of the Green Tuff were also presented by Liszewska *et al.* (2018) for matrix glasses and Romano *et al.* (2019) for melt inclusions; both resulted in nearly identical fractionating assemblages, with the model of Romano *et al.* (2019) resulting in a similar melt fraction (0.274) and the model of Liszewska *et al.* (2018) resulting in a much lower melt fraction (0.073).

For differentiation beyond the average glass composition to the precursor air-fall tuff, an additional mass balance model was calculated that replicates the "horizontal trend" of Liszewska *et al.* (2018) of declining FeO^T and Or at near-constant Qz^* and Al_2O_3 (Model C, $\Sigma r^2 = 0.613$). This model requires an additional 6% crystallization ($F = 0.94$) of an assemblage of aenigmatite (0.04) with alkali feldspar as the remainder. Liszewska *et al.*'s (2018)

Table 6: Representative olivine analyses

Group:	Altura	Cuddia Mida		
Sample ID:	060522	090512	060501	
Point:	#44	74 / 1.	#85	#110
SiO_2, wt%	30.25	28.92	28.88	28.74
FeO^T	58.51	64.80	64.60	67.18
MnO	4.78	3.61	4.38	4.16
MgO	6.32	0.65	2.33	1.03
CaO	0.33	0.29	0.70	0.47
Total	100.19	98.26	100.89	101.59
Formula (M_2TO_4)				
Si (T)	0.982	0.994	0.965	0.964
Fe^{2+}	1.588	1.863	1.805	1.885
Mn	0.132	0.105	0.124	0.118
Mg	0.306	0.033	0.116	0.052
Ca	0.011	0.011	0.025	0.017
ΣM	2.037	2.012	2.070	2.072
X-Fa	0.8335	0.9826	0.9276	0.9649
X-Fo	0.1606	0.0174	0.0595	0.0264
X-La	0.0060	0.0056	0.0129	0.0087

Components: Fo, Forsterite; Fa, Fayalite; La, Larnite

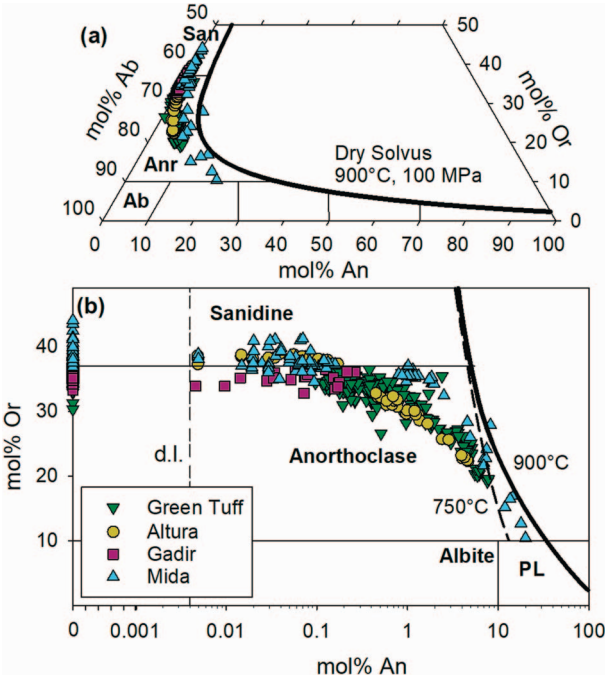

Fig. 8. (a) Classification of feldspars (Table 4, Supplementary Table S4) shown with the 900°C, 100 MPa dry solvus calculated with SolvCalc (Wen & Nekvasil, 1994) using the solution model of Nekvasil & Burnahm (1987). Ab, Albite; Anr, Anorthoclase; San, Sanidine. (b) A semi-log plot of mol% Or versus mol% An (with the 900° and 750°C solvi) that displays anorthoclase compositions in greater detail. GT data are from Liszewska *et al.* (2018). The vertical dashed line indicates the approximate detection limit (d.l.); note that values with <0.001 mol% An are plotted on a linear scale and all samples with CaO below the detection limit are plotted at 0. PL, Plagioclase.

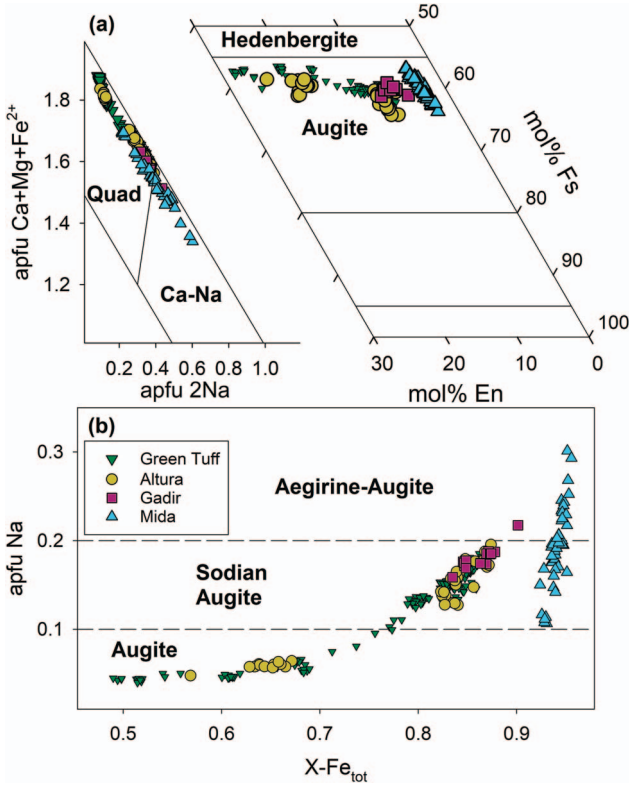

Fig. 9. (a) Classification of clinopyroxenes (Table 5, Supplementary Table S5) following Morimoto (1989). (b) Atoms per formula unit [apfu] Na plotted versus X-Fe_{tot} [= apfu Fe^T / (Fe^T + Mg)] for the clinopyroxenes. in T-ΔNNO space.

model for the horizontal trend requires a similar amount of additional crystallization (8%, F = 0.92) mostly of aenigmatite (0.04) and quartz (0.03), with trace amounts of clinopyroxene (0.01) and alkali feldspar (<0.01).

Cala dell'Altura volcanic Centre

Two models are presented for Altura: Model D describes fractionation along the LLOD between comenditic trachyte (sample 060522; 13.1 wt% Qz*, 917 μg/g Zr, P.I. = 1.1) and pantellerite (sample

Table 7: Representative aenigmatite analyses

Group:	Cala dell'Altura		Gadir	Cuddia Mida		
Sample:	**150532**	**150533**	**190532**	**090512**	**090511**	**090514**
Point:	**sub plate**	**1**	**7 / 1.**	**67 / 1.**	**1 / 1.**	**42 / 1.**
SiO_2, wt%	41.27	40.92	40.503	40.83	40.10	40.30
TiO_2	9.01	9.03	9.137	9.04	8.87	8.80
Al_2O_3	0.52	0.52	0.822	0.43	0.37	0.29
FeO^T	39.50	39.85	40.716	41.12	41.23	40.97
MnO	1.41	1.40	1.343	1.23	1.09	1.21
MgO	0.95	0.90	0.918	0.42	0.40	0.38
CaO	0.53	0.43	0.657	0.38	0.41	0.28
Na_2O	6.87	7.20	6.869	6.95	6.88	7.00
Total	100.06	100.25	100.97	100.39	99.34	99.23
Recalculated FeO^T						
Fe_2O_3	1.03	3.24	3.18	2.33	3.29	3.36
FeO	38.57	36.94	37.86	39.02	38.27	37.94
Total	100.16	100.57	101.28	100.62	99.67	99.57
X-Ti	0.17	0.17	0.17	0.17	0.16	0.16
Formula $(Na,Ca)_2M_5(Ti,Fe^{3+})T_6O_{20}$						
Si	5.884	5.810	5.732	5.830	5.789	5.817
^{IV}Al	0.087	0.087	0.137	0.073	0.064	0.049
$^{IV}Fe^{3+}$	0.028	0.103	0.131	0.098	0.147	0.133
$\sum T$	6.000	6.000	6.000	6.000	6.000	6.000
Ti	0.966	0.964	0.972	0.970	0.963	0.955
$^{VI}Fe^{3+}$	0.034	0.036	0.028	0.030	0.037	0.045
$\sum(Ti, Fe^{3+})$	1.000	1.000	1.000	1.000	1.000	1.000
^{VI}Al	0.000	0.000	0.000	0.000	0.000	0.000
$^{VI}Fe^{3+}$	0.049	0.208	0.180	0.123	0.173	0.187
Fe^{2+}	4.599	4.386	4.481	4.659	4.621	4.579
Mn	0.170	0.168	0.161	0.148	0.133	0.148
Mg	0.202	0.191	0.194	0.089	0.085	0.081
^{VI}Ca	0.000	0.048	0.000	0.000	0.000	0.004
$\sum M$	5.020	5.000	5.016	5.019	5.012	5.000
^{VIII}Ca	0.081	0.018	0.100	0.058	0.063	0.040
Na	1.899	1.982	1.885	1.923	1.925	1.960
$\sum(Na,Ca)$	1.980	2.000	1.984	1.981	1.988	2.000

X-Ti = mol Ti / (Ti + Fe^T). Iron recalculated with charge balance. Formula recalculation following Kunzmann (1999) and Grew *et al.* (2008).

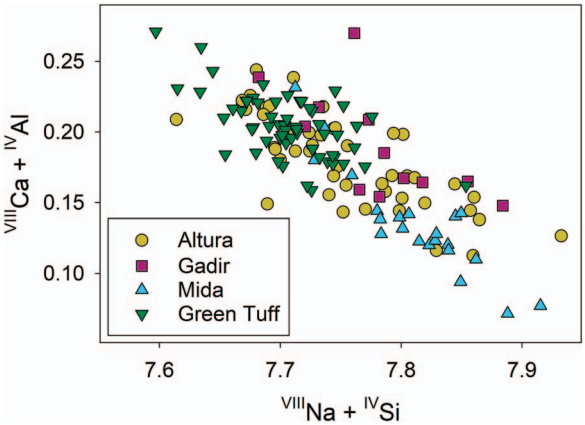

Fig. 10. Extent of the substitution $Ca^{2+} + Al^{3+} = Na^+ + Si^{4+}$ in aenigmatite. Data from Table 7 and Supplementary Table S7. GT data are from Liszewska *et al.* (2018).

150 532; 38.8 wt% Qz*, 2067 μg/g Zr., P.I. = 1.6); Model E describes fractionation within that pantellerite sample from the whole-rock analysis to an analysis of evolved glass (42.3 wt% Qz*, P.I. = 1.69) with slightly higher SiO_2 and lower FeO^T and CaO. Model D has a very good fit ($\Sigma r^2 = 0.166$) with a melt fraction of 0.420 (58% crystallization) and suggests a LLOD that was the result of fractionation of an assemblage similar to the Green Tuff with respect to alkali feldspar (0.53, or 90.5% of the fractionating assemblage), but with a different mafic assemblage with more clinopyroxene (0.04) and magnetite (0.015%) and only trace amounts (<0.01) of olivine and apatite. The model of the extended LLOD seen in glass analyses in the daughter sample (Model E) has an excellent fit ($\Sigma r^2 = 0.098$) and requires an additional 11% fractionation (F = 0.887) of alkali feldspar (0.08, or 65% of the fractionating assemblage), amphibole (0.04), and aenigmatite (<0.01).

Cala Gadir volcanic centre

Due to its limited exposure, very few whole-rock samples are available for Gadir and they are similar enough to preclude any opportunity to calculate a meaningful LLOD for this centre. A single model (G) is presented to describe fractionation between the whole-rock composition (37.6 wt% Qz*, 2117 μg/g Zr, P.I. = 1.3) and evolved glass (43.6 wt% Qz*, 3413 μg/g Zr, P.I. = 1.5), which has an excellent fit ($\Sigma r^2 = 0.019$) and predicts a melt fraction of 0.772 after fractionation of a mineral assemblage dominated by alkali feldspar (0.17, or 73% of the fractionating assemblage) and quartz

Table 8: Representative analyses of Fe-Ti oxides

Group:	Cala dell'Altura			Gadir	Cuddia Mida			
Sample:	060522	150532	150533	190532	090511	090512	090513	060501
Point:	Avg	2	1	8 / 1.	17 / 1.	68 / 1.	6 / 1.	#23
Class:	Mgt	Ilm	Ilm	Ilm	Ilm	Ilm	Mgt	Ilm
SiO_2, wt%	0.07	0.06	1.16	0.02	0.03	0.29	0.12	bdl
TiO_2	22.39	50.82	45.77	51.17	51.25	51.46	25.89	49.46
Al_2O_3	0.46	bdl	0.66	0.02	0.01	0.03	0.42	bdl
V_2O_3	n.a.	0.17	0.25	0.18	0.25	0.25	0.13	n.a.
Cr_2O_3	0.04	n.a.	n.a.	0.04	0.01	0.03	0.01	0.14
FeO^T	69.96	45.73	44.07	46.02	45.31	46.30	67.70	46.25
MnO	1.94	2.54	0.62	2.41	1.91	1.98	1.70	2.12
MgO	0.40	0.14	0.21	0.16	0.08	0.10	0.25	0.15
CaO	0.06	0.04	0.64	0.03	0.01	0.03	0.01	n.a.
Nb_2O_5	n.a.	0.77	n.a.	0.90	0.52	0.27	0.09	n.a.
Total	95.32	100.27	93.38	100.95	99.38	100.73	96.31	98.11
Recalculated FeO^T								
Fe_2O_3	23.67	3.21	4.90	3.03	1.43	2.48	16.80	4.62
FeO	48.66	42.84	39.66	43.29	44.03	44.07	52.59	42.09
Total	97.69	100.53	92.71	101.23	99.49	100.69	97.99	98.58
Formula (Ilm: M_2O_3, Mgt: M_3O_4)								
O	4.000	3.000	3.000	3.000	3.000	3.000	4.000	3.000
Si	0.003	0.002	0.031	0.001	0.001	0.007	0.004	0.000
Ti	0.645	0.963	0.919	0.963	0.980	0.968	0.742	0.954
Al	0.021	0.000	0.021	0.001	0.000	0.001	0.019	0.000
V	—	0.003	0.005	0.004	0.005	0.005	0.004	—
Cr	0.001	—	—	0.001	0.000	0.001	0.000	0.003
Fe^{3+}	0.683	0.042	0.074	0.036	0.015	0.034	0.479	0.089
Fe^{2+}	1.560	0.921	0.909	0.927	0.949	0.935	1.680	0.902
Mn	0.063	0.054	0.014	0.051	0.041	0.042	0.014	0.046
Mg	0.023	0.005	0.008	0.006	0.003	0.004	0.000	0.006
Ca	0.002	0.001	0.018	0.001	0.000	0.001	0.001	—
Nb	—	0.009	0.000	0.010	0.006	0.003	0.000	—
∑M	3.000	2.000	2.000	2.000	2.000	2.000	2.945	2.000
X-Usp	0.6487	—	—	—	—	—	0.7491	—
X-Ilm	—	0.9678	0.9540	0.9696	0.9855	0.9754	—	0.9530

Class: Mgt, Magnetite; Ilm, Ilmenite. Oxides recalculated following Andersen *et al.* (1993) with total iron (FeO^T) recalculated following Carmichael (1967).
Formula: ΣM, Sum of Cations. Components: Usp, Ulvöspinel; Ilm, Ilmenite.

(0.05), with amphibole (0.02) as the main mafic phase along with trace ilmenite.

Cuddia Mida volcanic Centre

For whole-rock samples that lie in the 'thermal valley', an LLOD can be calculated only for a pantellerite with 32.5 wt% Qz*, 1640 μg/g Zr, and P.I. = 1.6 (090512) to pantellerite on the feldspar-quartz cotectic with 39.2 wt% Qz*, 1986 μg/g Zr, and P.I. = 1.9 (090513). The resulting model (H) has an excellent fit ($\Sigma r^2 = 0.094$) with a melt fraction of 0.820 and a fractionating assemblage of alkali feldspar (0.16, or 84% of the assemblage) with subequal amounts (~0.02 each) of amphibole and aenigmatite, similar to the observed modal assemblage. Mass balance models were also calculated for fractionation from the whole-rock (090512) composition to glass with 46.7 wt% Qz*, 3109 μg/g Zr, and P.I. = 2.5 (model J) and to one of the most evolved glasses with 56.2 wt% Qz*, 3576 μg/g Zr, and P.I. = 3.2 (model K). Both models have an acceptable fit ($\Sigma r^2 = 0.072$ and 0.470, respectively) and similar results with varying mineral proportions, as would be expected from compositions lying on the same LLOD. with relatively low melt fractions (decreasing from 0.647 to 0.437) and a fractionating assemblage dominated by alkali feldspar (increasing from 0.29 to 0.43, 80–76% of the fractionating assemblage) and quartz (increasing from 0.02 to 0.08), with lesser amounts of amphibole (0.02–0.03), aenigmatite (0.02), trace (<0.01) apatite, and a negligible amount of clinopyroxene. The diminished role for clinopyroxene and greater role for quartz in this assemblage is consistent with the observed positive correlation of Qz* with CaO and negative correlation of Qz* and SiO_2 in this series. A model (L) of fractional crystallization from a glass analysis in sample 090512 with 45.6 wt% Qz*, 2413 μg/g Zr, and P.I. = 2.0 to the same highly evolved composition requires 36% crystallization (F = 0.65) of an assemblage only alkali feldspar (0.26, or 70% of the fractionating assemblage) and quartz (0.11), highlighting the that extreme fractionation to the EMC may require not just an assemblage of alkali feldspar ± quartz but also a dearth of mafic phases (*cf.* LeMasurier *et al.*, 2018).

Summary

Mass-balance modelling confirms that all suites evolved from trachyte to pantellerites with compositions that plot near the experimental (*viz.*, Carmichael & MacKenzie, 1963) whole-rock

Table 9: Representative amphibole analyses

Group:	Cala dell'Altura				Gadir		Cuddia Mida			
Sample ID:	150532		150533		190 532		090514	090513	060501	060502
Point:	200 x 180 μm euh		875 x 420 μm prism		14 / 1.	21 / 1.	29 / 1 .	1 / 1.	#28	#46
	Core	Rim	Core	Rim						
SiO_2, wt%	48.87	48.89	48.63	48.80	49.23	48.90	47.68	47.54	48.45	47.78
TiO_2	2.01	2.31	1.98	2.24	1.73	2.09	1.87	1.49	1.42	1.88
Al_2O_3	1.32	1.18	1.58	1.33	1.48	1.38	0.68	0.54	0.57	0.81
FeO^T	27.89	29.36	26.13	29.12	26.83	29.00	32.58	33.50	34.21	33.18
MnO	1.22	1.26	1.10	1.21	1.18	1.23	1.13	1.05	1.27	1.21
MgO	5.21	4.27	6.41	4.31	5.95	4.38	1.44	1.26	1.70	1.41
CaO	6.07	5.60	6.46	5.89	5.94	5.55	4.78	4.23	4.08	4.61
Na_2O	5.06	5.15	5.08	5.13	5.22	5.18	5.41	5.66	5.56	5.33
K_2O	1.08	1.13	0.94	1.12	0.98	1.05	1.40	1.57	1.31	1.30
H_2O^+	n.a.	n.a.	n.a.	n.a.	1.43	1.58	1.57	n.a.	n.a.	n.a.
F	1.35	1.54	1.87	1.47	0.98	0.65	bdl	bdl	1.46	1.29
Cl	0.08	0.07	0.07	0.07	0.06	0.07	0.06	0.05	0.06	0.06
Sum	100.16	100.76	100.25	100.69	101.01	101.05	99.09	97.44	100.09	98.84
O=F,Cl	0.59	0.66	0.80	0.63	0.43	0.29	0.01	0.01	0.63	0.56
Total	99.57	100.10	99.45	100.06	100.58	100.76	98.86	97.20	99.46	98.28
Recalculated FeO^T										
Fe_2O_3	1.24	1.40	1.19	1.10	1.43	1.42	0.87	2.38	2.59	1.51
FeO	26.77	28.10	25.06	28.13	25.54	27.72	31.80	31.36	31.89	31.82
Total	99.70	100.24	99.57	100.17	100.72	100.90	98.95	98.98	99.72	98.44
X-Fe_{tot}	0.75	0.79	0.69	0.79	0.72	0.79	0.93	0.94	0.92	0.93
Formula ($A_{0\text{-}1}B_2C_5T_8O_{22}X_2$)										
Si	7.606	7.620	7.544	7.608	7.621	7.631	7.761	7.756	7.747	7.729
^{IV}Al	0.242	0.217	0.289	0.244	0.269	0.254	0.130	0.103	0.108	0.153
^{IV}Ti	0.152	0.163	0.168	0.148	0.109	0.115	0.109	0.141	0.145	0.118
ΣT	8.000	8.000	8.001	8.000	7.999	8.000	8.000	8.000	8.000	8.000
^{VI}Ti	0.083	0.108	0.063	0.115	0.092	0.130	0.120	0.042	0.026	0.111
$^{VI}Fe^{3+}$	0.145	0.163	0.140	0.128	0.166	0.168	0.106	0.293	0.310	0.184
Mn	0.078	0.073	0.064	0.087	0.060	0.067	0.095	0.081	0.000	0.060
Fe^{2+}	3.485	3.664	3.249	3.669	3.307	3.617	4.330	4.278	4.259	4.305
Mg	1.209	0.992	1.482	1.002	1.374	1.018	0.350	0.306	0.405	0.340
∑C	5.000	5.000	4.998	5.001	4.999	5.000	5.001	5.000	5.000	5.000
Mn	0.083	0.093	0.080	0.073	0.095	0.096	0.060	0.064	0.172	0.105
Fe^{2+}	0.000	0.000	0.000	0.000	0.000	0.000	0.000	0.000	0.006	0.000
Ca	1.012	0.935	1.074	0.984	0.985	0.928	0.834	0.740	0.700	0.799
Na	0.905	0.972	0.846	0.943	0.920	0.975	1.106	1.196	1.121	1.096
ΣB	2.000	2.000	2.000	2.000	2.000	1.999	2.000	2.000	1.999	2.000
Na	0.622	0.585	0.682	0.607	0.645	0.593	0.600	0.595	0.601	0.576
K	0.214	0.225	0.186	0.223	0.193	0.208	0.291	0.327	0.267	0.268
ΣA	0.836	0.810	0.868	0.830	0.838	0.801	0.891	0.922	0.868	0.844
ΣT,C,B,A	15.836	15.810	15.867	15.831	15.836	15.800	15.892	15.922	15.867	15.844
OH	1.314	1.222	1.064	1.257	1.504	1.662	1.983	1.986	1.247	1.325
F	0.664	0.759	0.917	0.725	0.479	0.319	—	—	0.737	0.660
Cl	0.021	0.018	0.018	0.018	0.017	0.019	0.017	0.014	0.015	0.015
ΣX	2.000	2.000	2.000	2.000	2.000	2.000	2.000	2.000	1.999	2.000

Amphibole recalculated following Hawthorne *et al.* (2012) with the MS Excel spreadsheet of Locock (2014). FeO^T, total iron reported as FeO; X-Fe_{tot} = mol $Fe^T/(Mg + Fe^T)$

minimum *via* fractional crystallization of a similar assemblage dominated by alkali feldspar (~90% of the fractionating assemblage) with subordinate clinopyroxene, olivine, ilmenite, aenigmatite, and apatite. However, continued evolution to glass compositions beyond this point to the apparent minima for each suite require different assemblages that vary primarily by their mafic phases and the presence or absence of quartz. In the next section, we attempt to relate the paths to variable pre-eruptive conditions in the reservoirs.

Previous Geobarometric estimates

The depth of the basaltic reservoir beneath Pantelleria has been estimated to be 8–6 km (200–150 MPa) based both on H_2O-CO_2 equilibria in melt inclusions (Gioncada & Landi, 2010; Neave *et al.*, 2012) and thermodynamic modelling (White *et al.*, 2020). The application of various methodologies has consistently placed the silicic reservoirs at ≤6 km (≤150 MPa; Mahood, 1984; Lowenstern, J.B., 1994; Civetta *et al.*, 1998; White *et al.*, 2009; Di Carlo *et al.*, 2010; Gioncada & Landi, 2010; Neave *et al.*, 2012;

Table 10: Representative apatite analyses

Group:	Altura	Gadir	Cuddia Mida		
Sample ID:	**150533**	**190532**	**090512**	**090514**	**090513**
Point:		**22 / 1.**	**53 / 1.**	**46 / 1.**	**8 / 1 .**
SiO_2, wt%	2.39	2.25	2.09	1.06	0.45
FeO	0.38	0.50	0.65	0.55	0.57
MnO	0.00	0.13	0.09	0.18	0.13
MgO	0.02	0.00	0.00	0.02	0.02
CaO	49.75	47.90	51.98	53.07	55.39
Na_2O	0.62	0.59	0.56	0.32	0.17
P_2O_5	37.91	35.72	33.66	40.14	41.88
Y_2O_3	0.33	0.46	0.12	0.13	bdl
La_2O_3	1.37	1.79	1.97	0.86	0.30
Ce_2O_3	2.91	3.77	3.89	1.86	0.63
Pr_2O_3	n.a.	0.47	1.67	0.95	0.36
Nd_2O_3	n.a.	2.10	n.a.	n.a.	n.a.
H_2O	n.a.	0.24	0.58	0.55	n.a.
F	2.02	2.83	2.12	2.44	2.21
Cl	0.04	0.05	0.04	0.02	0.15
Sum	97.74	98.80	99.40	102.17	102.25
O=F, Cl	0.86	1.20	0.90	1.03	0.96
Total	96.88	97.59	98.50	101.13	101.29
Formula ($M_5(TO_4)_3X$)					
P	2.875	2.756	2.612	2.891	2.992
Si	0.214	0.205	0.191	0.091	0.038
ΣT	3.089	2.961	2.803	2.981	3.030
Ca	4.775	4.676	5.105	4.838	5.008
Fe	0.028	0.038	0.049	0.039	0.040
Mn	0.000	0.010	0.007	0.013	0.010
Na	0.108	0.105	0.099	0.053	0.028
Y	0.016	0.023	0.006	0.006	0.000
La	0.045	0.060	0.066	0.027	0.009
Ce	0.095	0.126	0.130	0.058	0.020
Pr	—	0.015	0.056	0.030	0.011
Nd	—	0.068	—	—	—
ΣM	5.068	5.121	5.519	5.064	5.126
F	0.572	0.816	0.615	0.657	0.590
Cl	0.006	0.007	0.005	0.003	0.021
OH	0.422	0.177	0.379	0.340	0.389
ΣX	1.000	1.000	1.000	1.000	1.000

Apatite analyses recalculated following Pasero *et al.* (2010)

Lanzo *et al.*, 2013; Arzilli *et al.*, 2020; Stabile *et al.*, 2021; Romano *et al.*, 2021). Many of these studies have, at least in part, relied on equivocal results that rely on volatile contents and calculated solubilities that have placed the felsic reservoir for the Green Tuff at ≤4 km (≤100 MPa), based on maximum H_2O concentrations in melt inclusions up to 4.2 wt% (Lanzo *et al.*, 2013; Romano *et al.*, 2019), and between 2 and 6 km (50–150 MPa) for post-Green Tuff pantellerites, based on H_2O concentrations in melt inclusions between 2.5 and 4.9 wt% (Métrich *et al.*, 2006; Gioncada & Landi, 2010; Neave *et al.*, 2012). Neither Lowenstern & Mahood (1991) nor Gioncada & Landi (2010) detected any CO_2 by FTIR in melt inclusions by FTIR; however, Neave *et al.* (2012) reported concentrations (analyzed by SIMS) up to 150 ppm CO_2, which they used with H_2O data to calculate a depth of ~5.5 km (~146 MPa) for post-Green Tuff pantellerites. Lanzo *et al.* (2013) compared Cl concentrations in the Green Tuff (~1 wt%) and post-Green Tuff pantellerites (~0.85 wt%) with the experimental results of Métrich & Rutherford (1992) and Signorelli & Carroll (2002) and concluded that the Green Tuff reservoir may have been emplaced at a much shallower level (2–3 km, or 50–100 MPa) than the post-Green Tuff pantellerites (≥4.5 km, or ≥ 120 MPa). From their experimental results, Di Carlo *et al.* (2010) also placed the post-Green Tuff reservoir at 5 ± 1 km (120 ± 20 MPa). Based on this previous work, in the following section we will use values of 100 MPa and 150 MPa to calculate initial estimates of T and fO_2, and then use a new iterative technique to calculate a new estimate of P for fayalite-bearing rocks.

Mineral Equilibria

Carmichael (1962) and Nicholls & Carmichael (1969) noted that ilmenite is frequently the sole oxide in pantelleritic rocks, from which they deduced the reduced nature of these melts. They also described an apparent antipathetic relationship between oxides and aenigmatite with increasing melt peralkalinity and suggested the presence of a 'no-oxide' field in melts with high peralkalinity and lower temperatures crystallizing at oxygen fugacities above the fayalite-magnetite-quartz (FMQ) buffer. White *et al.* (2005) proposed a generalized 'reaction series' for pantellerite that was demonstrated experimentally by Romano *et al.* (2020). With increasing silica activity, peralkalinity (P.I. ~1.0 to 2.0) and

Table 11: Summary of the results of mass balance modelling

	Model Parent			Model daughter			Fractionating assemblage									Melt Fraction		
Model	**wt% Qz***	**P.I.**	**μg/g Zr**	**Qz***	**P.I.**	**Zr**	**Afs**	**Qz**	**Aen**	**Cpx**	**Amp**	**Ol**	**Ap**	**Ilm**	**Mgt**	**F**	**F(Zr)**	**$\sum r^2$**
Green Tuff Ignimbrite																		
(A1)	9.16	1.15	487	38.97	1.77	2021	0.64	—	0.01	0.03	—	0.03	<0.01	0.01	—	0.279	0.236	0.003
(A2)	9.16	1.15	487	44.53	1.84	2221	0.67	—	0.01	0.04	—	0.03	—	0.01	—	0.246	0.219	0.010
(B)	30.84	1.61	1634	44.53	1.84	2221	0.22	—	0.03	0.01	—	—	—	—	—	0.733	0.736	0.067
(C)	44.53	1.84	2221	43.78	1.79	2591	0.01	—	0.04	—	—	—	—	—	—	0.944	0.857	0.613
Cala dell'Altura Volcanic Centre																		
(D)	13.06	1.09	917	38.78	1.64	2067	0.54	—	—	0.04	—	<0.01	<0.01	—	0.02	0.420	0.444	0.166
(E)	38.78	1.64	2067	42.34	1.69	n.a.	0.08	—	0.01	—	0.04	—	—	—	—	0.887	n.a.	0.098
Cala Gadir Lava Dome																		
(G)	37.59	1.34	2117	43.58	1.50	3413	0.17	0.05	—	—	0.02	—	—	<0.01	—	0.772	0.620	0.019
Cuddia Mida Volcanic Centre																		
(H)	32.45	1.63	1640	39.22	1.91	1986	0.16	—	0.02	—	0.02	—	<0.01	—	—	0.820	0.826	0.094
(J)	32.45	1.63	1640	46.74	2.45	3109	0.29	0.02	0.02	<0.01	0.02	—	0.01	—	—	0.647	0.528	0.072
(K)	32.45	1.63	1640	56.17	3.17	3576	0.43	0.08	0.02	<0.01	0.03	—	<0.01	—	—	0.437	0.459	0.470
(L)	45.55	2.01	2413	56.17	3.17	3576	0.25	0.10	—	—	—	—	—	—	—	0.653	0.675	0.169

See text and Supplementary Table 10 for Model details. $Qz^* = 100Qz_n/(Qz_n + Or_n + Ab_n)$, subscript n indicates normative values (in wt%) calculated following Kelsey (1965) with iron oxides recalculated following Le Maitre (1976). P.I. (Peralkalinity Index) = mol (Na + K)/Al; Fractionating assemblage: Afs, alkali feldspar; Aen, aenigmatite; Cpx, clinpyroxene; Amp, amphibole; Ol, olivine; Qz, quartz; Ap, apatite; Ilm, ilmenite; Mgt, magnetite. F, calculated melt fraction. $F(Zr) = Zr_{Parent}/Zr_{Daughter}$ $\sum r^2$, sum of squares of residuals.

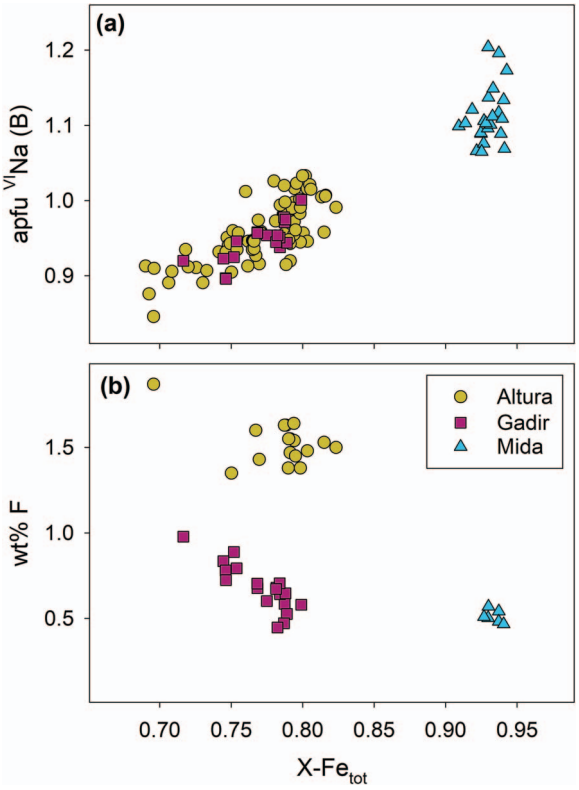

Fig. 11. X-Fe_{tot} [= apfu Fe^T / (Fe^T + Mg)] for the amphiboles plotted against (a) atoms per formula unit [apfu] Na occupying the octahedral (VI) B-site (on a 23 oxygen basis) and (b) wt% F. Data from Table 9 and Supplementary Table S9.

decreasing temperature (~900 to 700°C), the assemblages (each accompanied by alkali feldspar) are: (1) augite + olivine + ilmenite + magnetite, (2) sodian augite + fayalitic olivine + ilmenite; (3) sodian augite + fayalite + ilmenite + aenigmatite; (4) sodian augite + ilmenite + aenigmatite + quartz ± amphibole, and (5) aegirine-augite + aenigmatite + quartz ± amphibole. Rock samples from the magma series in this study have quartz-bearing assemblages (*viz.*, types 4 and 5) that plot on the alkali feldspar-quartz cotectic at or near the whole-rock minimum (or minima). Anomalous among these are two samples from Mida that have fayalitic ($Fa_{>95}$) olivine, and one that crystallized magnetite instead of ilmenite.

Here we use mineral equilibria to provide constraints on the pressure (P), temperature (T), and oxygen fugacity (fO_2) for the pre-eruptive conditions of these samples. These assemblages are evaluated using equilibria in the Ca-QUIlF system (Frost *et al.*, 1988; Frost & Lindsley, 1992; Lindsley & Frost, 1992) for reactions involving olivine, clinopyroxene, ilmenite, and quartz *via* use of the QUILF95 program (Andersen *et al.*, 1993), along with reactions between aenigmatite, ilmenite, and quartz (White *et al.*, 2005; Macdonald *et al.*, 2011; Romano *et al.*, 2020). For all calculations using the QUILF95 program, we use the results from Fe-Mg-Ca exchange for reactions involving silicates, but only Fe-Ti exchange for reactions involving silicates and oxides (*viz.*, ignoring Mg-Mn in oxides). All oxygen fugacity values are reported as log units relative to the nickel-nickel oxide (NNO) buffer (O'Neil & Pownceby, 1993; Pownceby & O'Neil, 1994). The full results of these calculations are presented in Supplementary Tables 12 and Supplementary Table 13 and discussed below.

Clinopyroxene-Ilmenite-Aenigmatite-quartz Equilibria

For assemblages with quartz, clinopyroxene, aenigmatite, and ilmenite but neither olivine nor magnetite, White (2011) proposed that temperature and oxygen fugacity can be estimated by calculating the intersection of two curves in T-fO_2 space, based on the assumption that all four phases equilibrated under the same conditions (*cf.* Berman, 1991):$2Fe_2Si_2O_6 + O_2 = 2Fe_2O_3 + 4SiO_2$,.

clinoferrosilite + O_2 = hematite + quartz.$Na_2TiFe_5Si_6O_{20} + O_2 = 2Fe_2O_3 + FeTiO_3 + Na_2Si_2O_5$ (melt) + $4SiO_2$,.

aenigmatite + O_2 = hematite + ilmenite + Nds + quartz.

Equation 1 is the displaced augite-hematite-quartz (AHQ) buffer, which is calculated using the QUILF95 program (Andersen *et al.*, 1993) to solve for fO_2 over a range of temperatures (660–760°C) for given values of X-Wo, X-En, and X-Hem at a stated pressure (with $aSiO_2$[Qtz] = 1.0 for quartz saturation). Equation 2 defines the position of the so-called 'no oxide' boundary proposed by White *et al.* (2005) and hereafter referred to as the displaced aenigmatite-ilmenite-quartz buffer (AenIQ), which is calculated over the same range of temperatures and at the same pressure for given values of X-Hem and X-Ilm with activities for these components also calculated using QUILF95 (oxide solution model of Andersen *et al.*, 1991), with unit values for $aSiO_2$[Qtz] and $aNa_2Si_2O_5$ (for P.I. > 1.0; Carmichael *et al.*, 1974, p. 288). The positions of these curves and their point of intersection are strongly pressure-dependent; therefore, we present and discuss results calculated at both 100 and 150 MPa (as described in the previous section). Temperatures calculated at 150 MPa versus 100 MPa are ~11°C lower; values for relative fO_2 stated in terms of ΔNNO are nearly identical. Likewise, rather than extrapolating conclusions based on calculations from arbitrary 'representative analyses' we use the entire range of ilmenite and clinopyroxene compositions to calculate parameters to define stability fields for these assemblages in T-fO_2 space (Fig. 12).

Altura. At 100 MPa, calculated temperatures range from 754°C to 713°C, declining with increasing X-Fe_{tot} and decreasing X-En in clinopyroxene (0.82–0.87 and 0.1174–0.0840, respectively). Calculated redox conditions are highly sensitive to ilmenite compositions (especially at values approaching end-member compositions) and range from ΔNNO-1.2 to −2.1 as the X-Hem component in ilmenite varies from 0.0460 to 0.0244. At 150 MPa, calculated oxygen fugacities are similar (ΔNNO-1.2 to −1.9) but temperatures are an average of ~42°C lower (711 to 671°C).

Gadir. Mineral compositions in the sample from Gadir are similar to Altura, and therefore result in similar T-fO_2 values. At 100 MPa, temperatures decrease from 737 to 711°C with increasing X-Fe_{tot} and decreasing X-En in clinopyroxene (0.84–0.90 and 0.1088–0.0676, respectively). Relative oxygen fugacity is between ΔNNO-1.3 (X-Hem = 0.0399) and − 2.3 (X-Hem = 0.0236). At 150 MPa, calculated T-fO_2 values range between 669–695°C and ΔNNO-1.1 to −2.1.

Mida. Calculated temperatures from Mida are similar to those from Altura and Gadir (715–762°C at 100 MPa and 674–721°C at 150 MPa). However, the presence of some ilmenite grains with ~99 mol% Ilm extends the calculated range of oxygen fugacities from ΔNNO-1.3 and − 1.5 (at X-Hem = 0.0363) to −3.3 (at X-Hem = 0.0128).

Geobarometry from olivine-Clinopyroxene-Ilmenite-Aenigmatite-quartz Equilibria

Olivine (92.6–97.6 mol% Fa) is found in two samples from Mida (090512 and 060501) in assemblages with clinopyroxene, ilmenite,

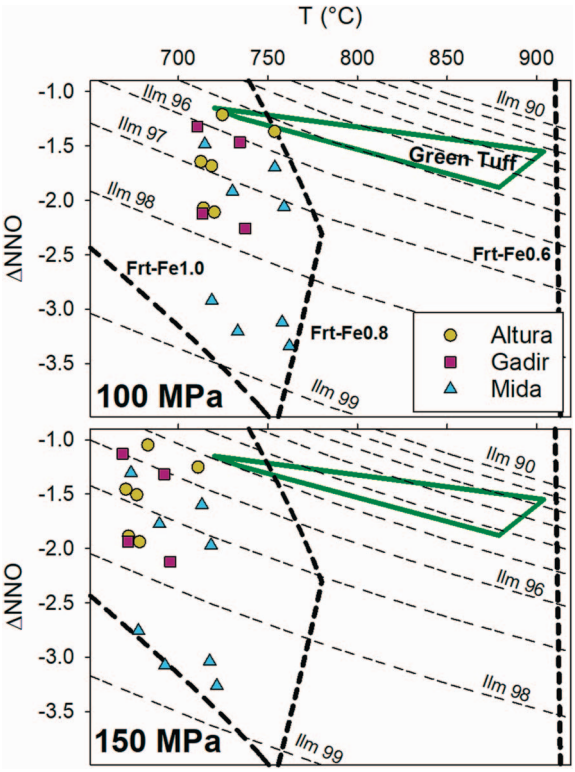

Fig. 12. Summary of the results of clinopyroxene-ilmenite-aenigmatite-quartz geothermometry (T, °C) and oxygen barometry (fO_2 plotted relative to the nickel-nickel oxide buffer (ΔNNO; O'Neil & Pownceby, 1993, Pownceby & O'Neil, 1994) at (a) 100 MPa and (b) 150 MPa with isopleths for ilmenite in equilibrium with aenigmatite and quartz (Andersen *et al.*, 1991; White *et al.*, 2005; Romano *et al.*, 2020). See text and Supplementary Table S12 for details. Also plotted in both is the range of values for the GT (Liszewska *et al.*, 2018; Romano *et al.*, 2018, 2020) and the curves showing the experimental stability limits for ferrorichterite with compositions of X-Fe_{tot} = 0.6, 0.8, and 1.0 (Charles, 1977), both at 100 MPa.

aenigmatite, and quartz. For the olivine-clinopyroxene-quartz sub-assemblage, the QUILF algorithm can be used to either: (1) calculate temperature and evaluate equilibrium between clinopyroxene and olivine as a function of pressure; (2) calculate pressure and evaluate equilibrium as a function of temperature; or (3) calculate pressure and temperature given an assumption of equilibrium (Andersen *et al.*, 1993). The addition of ilmenite to this sub-assemblage can then be used to calculate fO_2. Because the olivine-clinopyroxene-ilmenite-quartz and aenigmatite-ilmenite-quartz sub-assemblages are both quartz-saturated, it is possible to estimate the P–T-fO_2 of equilibration of the entire assemblage (Nicholls *et al.*, 1971). To do so, an initial temperature and oxygen fugacity are calculated from cpx-ol-q-ilm equilibrium at an arbitrary pressure (100 MPa.) These values are then applied to the AenIQ equation for silica activity (Romano *et al.*, 2020) to calculate a new pressure:

$$P = \frac{-5666.7 + T \bullet \left(2.133 - \frac{1}{4}\log fO_2 + \frac{1}{4}\log a_{Ilm} + \frac{1}{2}\log a_{Hem}\right)}{0.55} + 0.1, \quad \text{(Equation 3)}$$

where P is the pressure in MPa, T is the temperature in K, and log fO_2, a_{Ilm}, and a_{Hem} are output values calculated by QUILF95. The newly estimated pressure is then returned to the QUILF95 program to calculate new T-fO_2 iteratively until pressure convergence was achieved; these results are presented in Supplementary Table 13. For the two olivine-bearing samples from Mida, calculated pressures are 155 MPa (X-Hem = 0.0288; ΔNNO-1.7) and 160 MPa (X-Hem = 0.0128; ΔNNO-3.0) for sample 090512 and 159 MPa for sample 060501 (X-Hem = 0.470; ΔNNO-1.0), with temperatures of 684–683° and 674°C, respectively. Therefore, our results from mineral equilibria agree with experimental results of Di Carlo *et al.* (2010) and the chlorine solubilities and provides additional evidence that the magma reservoir for the Mida/Fastuca system was likely deeper (~150 MPa, or ~5.7 km) than the reservoir for the Green Tuff (≤100 MPa, or ≤ 3.8 km).

Comparison with experimental results

In addition to the early experiments on synthetic silica-over saturated (*viz.*, haplogranitic) peralkaline systems by Carmichael & MacKenzie (1963), Bailey & Schairer (1966), and Thompson & MacKenzie (1967), phase equilibria experiments have been performed on samples from natural peralkaline systems from Olkaria, Kenya (Scaillet & Macdonald, 2001, 2003), Eburru, Kenya (Scaillet & Macdonald, 2006), and Pantelleria (Di Carlo *et al.*, 2010; Arzilli *et al.*, 2020; Romano *et al.*, 2020, 2021; Stabile *et al.*, 2021). There have also been experimental studies on the stability of alkali amphiboles in general (Della Ventura *et al.*, 2005) and the richterite-ferrorichterite series specifically (Charles, 1975, 1977). In this section, experimental and modelling results are integrated to provide further information on the conditions of amphibole formation and extreme differentiation in the Pantescan suites.

Amphibole stability

Phase equilibria studies on the solid-solution series between richterite ($NaNaCaMg_5Si_8O_{22}(OH)_2$; X-$Fe_{tot}$ = 0.0) and ferrorichterite ($NaNaCaFe_5Si_8O_{22}(OH)_2$; X-$Fe_{tot}$ = 1.0) were performed by Charles (1975, 1977), who experimentally determined the stability of these amphiboles as a function of temperature and oxygen fugacity. These experiments showed that at 100 MPa the magnesian endmember is stable up to 1025 ± 5°C at all values of fO_2 whereas the ferroan endmember has a maximum stability of 760 ± 10°C at fO_2 equivalent to the wüstite-magnetite (WM) buffer (~ΔNNO-4.2), falling to 535 ± 10°C at fO_2 equivalent to the fayalite-magnetite-quartz (FMQ) buffer (~ΔNNO-0.8). For compositions more like the most ferrous amphiboles from Altura and Gadir (X-Fe_{tot} = 0.8) maximum stability occurs at 780 ± 10°C at fO_2 equivalent to the C-CH_4 buffer (~ΔNNO-2.3), falling to 730 ± 10°C at fO_2 equivalent to the FMQ buffer (~ΔNNO-0.7). Temperatures and oxygen fugacities for the amphibole-bearing samples estimated from mineral equilibria at 150 and 100 MPa, along with the range of reported T-fO_2 for the Green Tuff (White *et al.*, 2009; Liszewska *et al.*, 2018; Romano *et al.*, 2020), are plotted with the stability fields of Charles (1977) in Figs 12a and b. Calculated T-fO_2 values for these samples and the compositions of their amphiboles (X-Fe_{tot} = 0.69–0.83 for Altura and Gadir; X-Fe_{tot} = 0.91 to 0.97 for Mida) are consistent with the experimental results of Charles (1977) and therefore support the interpretation of equilibration at both low temperatures (<750°C) and oxygen fugacities (<ΔNNO-1.0). The amphibole-free Green Tuff equilibrated at temperature and redox conditions greater than those for these amphiboles, but still well within the range of richterites with X-Fe_{tot} = 0.6–0.8 (<910 ± 10°C), which suggests that something other than favorable T and fO_2 may be required to stabilize this phase under these conditions.

Experiments on pantellerites have crystallized amphiboles using starting material from the Serra della Fastuca pumice (Di Carlo *et al.*, 2010; Romano *et al.*, 2020), Eburru pantellerite (Scaillet & Macdonald, 2006), and curiously in Green Tuff pumice (Romano *et al.*, 2020) despite its absence in natural samples.

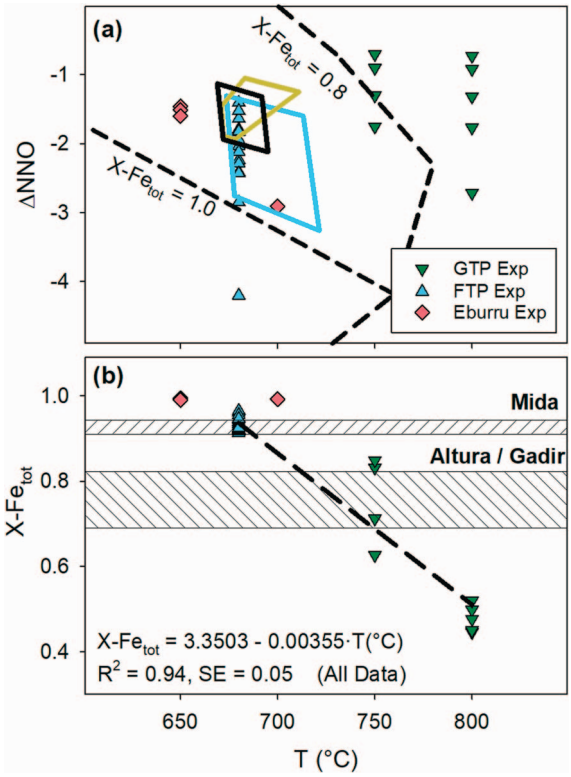

Fig. 13. (a) The ranges of T-fO_2 (relative to ΔNNO) for the amphibole-bearing pantellerites calculated at 150 MPa from mineral equilibrium (from Fig. 12) plotted with the experimental stability limits for ferrorichterite with compositions of X-Fe_{tot} = 1.0 and 0.8 (Charles, 1977) and the experimental conditions that resulted in the crystallization of amphibole for the GT pumice (GTP; Romano *et al.*, 2020) and the Fastuca pumice (FTP;Di Carlo *et al.*, 2010 ; Romano *et al.*, 2020). (b) Experimental amphibole compositions (as X-Fe_{tot}) from Di Carlo *et al.* (2010) and Romano *et al.* (2020) plotted versus temperature (T, °C) along with the range of natural amphibole compositions from this study.

Scaillet & Macdonald (2006) synthesized arfvedsonite at 150 MPa under water-rich conditions and oxygen fugacities (fO_2) equivalent to two log units below the nickel-nickel oxide buffer (ΔNNO-2) from a pantellerite from Eburru centre, Kenya. Sodic ($Na_B > 1.0$) and ferroan (X-$Fe_{tot} > 0.9$) amphiboles similar in composition to Mida were synthesized by Scaillet & Macdonald (2001, 2006), Di Carlo *et al.* (2010), and Romano *et al.* (2020) over a wide range of pressures (50–150 MPa) and water contents (1.8–6.0 wt% H_2O_m) but always at low oxygen fugacity (<ΔNNO-1.0) and temperature (<700°C), consistent with the results of Charles (1975, 1977). Amphiboles crystallized from the Green Tuff pumice range in composition from richterite (X-Fe_{tot} = 0.45–0.52) to ferrorichterite (X-Fe_{tot} = 0.63–0.85) at temperatures of 800°C and 750°C, respectively, in experiments conducted at 100 MPa and between ΔNNO-0.5 and −2.5 with 2.5–4.5 wt% H_2O_m. The compositions of the experimentally derived amphiboles from these experiments are consistent with the buffered experiments of Charles (1977) and overlap in T-fO_2 space with the values for the natural samples calculated from mineral equilibria at 150 MPa (Fig 13a).

Romano *et al.* (2020) have drawn attention to the difficulties in determining the stability of amphibole in pantellerites, partly because of their scarce occurrence and wide compositional range. Factors which have been invoked include high fF_2 (Ernst, 1962; Conrad, 1984; Scaillet & Macdonald, 2001, 2006; Di Carlo *et al.*, 2010; Giesting & Filiberto, 2014; Scaillet *et al.*, 2016), and relatively high melt Na contents (Romano *et al.*, 2020). Fluorine contents in amphiboles that formed at 680°C and 100 MPa are 0.78–0.86 wt% (Romano *et al.*, 2020), higher than natural ones from Mida (0.47–0.57 wt% F). In samples of the naturally amphibole-free Green Tuff pumice, Romano *et al.* (2020) synthesized amphiboles more similar in composition to Altura and Gadir (X-Fe_{tot} ≈ 0.63–0.85, Na_B ≈ 0.85–1.00) at temperatures of 750° and 800°C at 100 MPa under similar to slightly more oxidizing conditions (<ΔNNO-0.5) over a wide range of H_2O_m (1.3–4.5 wt%). These experimental amphiboles are higher in F (1.0–2.4 wt%), similar to the Altura and Gadir amphiboles (0.5–1.8 wt% F), reinforcing the proposition that high fluorine contents may stabilize amphibole at higher temperatures.

There is a strong (R^2 = 0.94) correlation between X-Fe_{tot} and temperature in amphiboles crystallized in the experiments of Di Carlo *et al.* (2010), Romano *et al.* (2020), and Scaillet & Macdonald (2006) (Fig. 13b) that may be used to estimate the temperature of crystallization in the natural samples. Amphiboles in Altura and Gadir samples suggest temperatures declining from 750° to 710° and 743° to 720°C, respectively, both overlapping with the range of temperatures estimated from clinopyroxene-ilmenite-aenigmatite-quartz equilibrium at 100 MPa, which may indicate that these phases co-saturated over this temperature interval. Amphiboles from Mida, however, have much higher X-Fe_{tot}, with values nearly identical to their experimental counterparts from Fastuca, suggesting crystallization at temperatures between 680° and 690°C, in agreement with values determined from mineral equilibria above. The higher A-site occupancy in the Mida amphiboles relative to both Altura and Gadir is also consistent with equilibration at lower oxygen fugacities for that former compared to the latter (Della Ventura *et al.*, 2005).

Fayalite, Aenigmatite, and quartz stability

White *et al.* (2005), Macdonald *et al.* (2011), and Romano *et al.* (2020) described an antipathetic relationship between fayalite and aenigmatite, with the two phases coexisting in equilibrium on a univariant curve in T-aSiO_2 space at constant P and ΔNNO. In experiments on metaluminous and peralkaline (comenditic) trachyte (Romano *et al.*, 2018), olivine (Fa_{57} to Fa_{88}) has been found to be stable over a wide range of pressures (50–150 MPa), temperatures (750–950°C), and oxygen fugacities (although under reducing conditions, <ΔNNO-0.6), with fayalite contents that positively correlate with the P.I. of the coexisting glass. In experiments on pantellerites, olivine has been a more elusive phase that has only been synthesized in the experiments of Romano *et al.* (2020), which crystallized fayalitic olivine ($Fa_{90–93}$) at 750°C, 100 MPa, and ΔNNO-1.3 to −1.9; at ΔNNO-1.9 fayalite co-precipitated with aenigmatite, and under more reducing conditions (ΔNNO-2.4) aenigmatite crystallized without fayalite. In these experiments (Di Carlo *et al.*, 2010; Romano *et al.*, 2020), aenigmatite crystallized under reducing conditions (<ΔNNO-1.0) at temperatures between 725 and 680°C and pressures between 100 to 150 MPa. Under more reducing conditions (≤ΔNNO-2.4) aenigmatite crystallized at temperatures as high as 750°C at pressures of 50 to 150 MPa.

Fayalite is stable in pantelleritic melts until the silica activity relative to quartz saturation (aSiO_2[Qtz]) is near unity, at which point aenigmatite (±quartz) begins to crystallize instead; at pressures of 100 MPa this occurs at ~750°C, when the P.I. of the melt is ~1.6 (White *et al.*, 2005; Macdonald *et al.*, 2011; Romano *et al.*, 2020). However, in some pantellerites—such as our samples from Mida and pantellerites from Eburru (Ren *et al.*, 2006)—fayalite and aenigmatite are in equilibrium to ~680°C and the P.I. of the melt is ~2.0. It has long been understood that olivine stability

in silicic magmas is favored at lower silica activities (Carmichael *et al.*, 1970; White *et al.*, 2005; Macdonald *et al.*, 2011) and that silica activity is inversely proportional to total pressure in magma (Nicholls *et al.*, 1971), so it stands to reason that the stability field of fayalite would be expanded to lower temperatures at higher pressures as our geothermobarometric calculations suggest. Additional evidence in support of this conclusion comes from experimental relations in comendites, in which fayalite crystallized only at P ≥ 150 MPa and ΔNNO-1.4 to −3.2 at temperatures as low as 661°C (Scaillet & Macdonald, 2001, 2003).

Glass compositions

The compositions of glasses from experiments conducted on the pantelleritic Green Tuff Pumice (GTP; Romano *et al.*, 2020), the pantelleritic Fastuca della Serra Pumice (FTP; Di Carlo *et al.*, 2010; Romano *et al.*, 2020), and the Eburru pantellerite (EBU; Scaillet & Macdonald, 2006) are plotted in Fig. 13 along with LLOD curves regressed through the natural data for the Green Tuff and Mida datasets (see Fig. 6). Experimental glasses from GTP runs have low FeO^T (Figure 14a) and are displaced along the feldspar-quartz cotectic to lower values of Or/(Or + Ab) (Figure 14b) than the main Green Tuff trend. This is certainly due to the nature of the starting material, a sample of the precursor air fall deposit of the Green Tuff that has a whole-rock composition similar to these glasses, which Liszewska *et al.* (2018) suggested resulted from late fractionation of aenigmatite > quartz > clinopyroxene > alkali feldspar (summarized in our Table 11). Therefore, although the experimental results from GTP can inform our understanding of the stability of amphibole and other phases, the whole-rock composition appears to represent an endpoint of a particular LLOD and will not be discussed further. FTP and EBU, on the other hand, have starting compositions that lie in the thermal valley and near the whole-rock minimum, respectively. The Mida glasses lie plot along the FTP trend, reaching the effective minimum composition. The phenocryst assemblage in the pumice is alkali feldspar, aenigmatite and clinopyroxene, with fayalite, amphibole and quartz occurring in minor amounts (Di Carlo *et al.*, 2010; Romano *et al.*, 2020) comparable to that in the Cuddia Mida rocks. Experimental FTP glasses with compositions approaching the EMC were performed at a wide range of pressures (50–150 MPa) and temperatures (725–800°C) but all required low relative oxygen fugacities (<ΔNNO-3). Proportions of glass (melt), alkali feldspar, and quartz in all runs vary similarly with Qz* regardless of P–T-fO_2, with values that agree with those predicted by mass balance models K and L for the Mida glass trend (Figure 15a). With respect to FeO^T, however, only runs conducted at lower oxygen fugacities generally crystallized lesser (<4%) proportions of mafic minerals, which enabled iron enrichment also predicted by the mass balance models (Figure 15b). One notable exception to this is a single run (9–7; Di Carlo *et al.*, 2010) at 680°C, 150 MPa, and ≤ ΔNNO-2.2 that has 21% amphibole and a very low melt fraction (0.03) that drove the melt composition to lower values of both Qz* and FeO^T and may represent near-solidus conditions.

Summary

Evidence from equilibria in the natural mineral assemblages and the experimental results suggests similarly low (670–700°C) minimum temperatures for all three amphibole-bearing units, lower than those determined for the amphibole-free Green Tuff (~720°C). Oxygen fugacity is also systematically lower (between ΔNNO-1.2 and −3.3) for amphibole-bearing units compared to amphibole-free systems, with the most reduced oxygen fugacities also associated with the most extreme glass compositions.

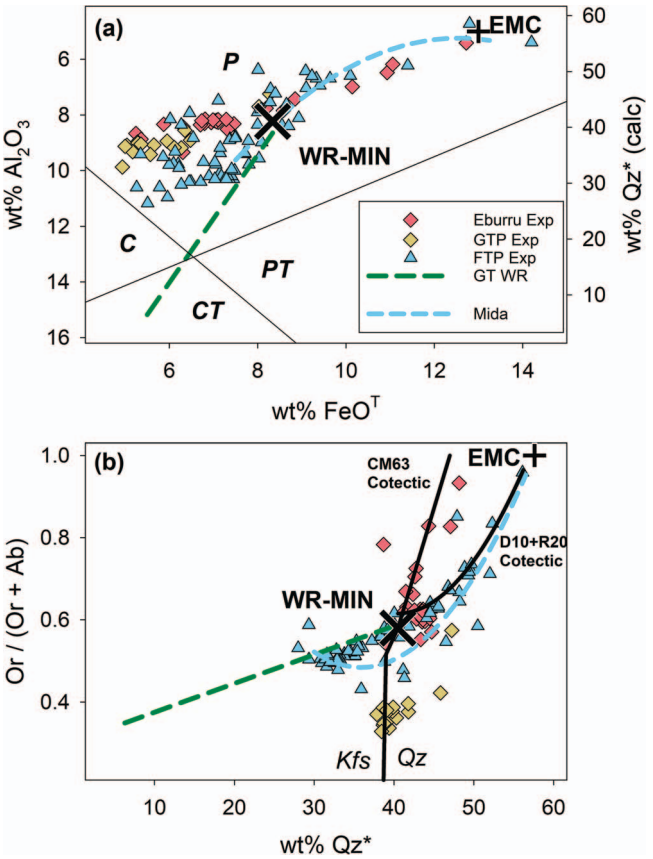

Fig. 14. (a) Experimental glasses from Eburru (Scaillet & Macdonald, 2006), GTP (Romano *et al.*, 2020), and FTP (Di Carlo *et al.*, 2010; Romano *et al.*, 2020) plotted on a modified Macdonald (1974) diagram with the natural GT and Mida trends (regressed through the data in Fig. 6) shown with the whole-rock minimum (WR-MIN) and effective minimum composition (EMC). (b) The isobaric projection of Fig. 6a re-plotted in a cartesian system (*cf.* Wilke *et al.*, 2017) with the ternary minimum and alkali feldspar-quartz cotectic from Carmichael & MacKenzie (1963) [CM63] and a new cotectic calculated from the results of Di Carlo *et al.* (2010) and Romano *et al.* (2020) [D10 + R20].

Implications for silicic peralkaline systems

Numerous studies have concluded that silicic peralkaline rocks form by protracted fractional crystallization of alkali basalts, along LLOD that include mugearite, benmoreite, and metaluminous trachyte (Macdonald *et al.*, 2021, and references therein). Whether metaluminous trachyte continues to evolve *via* fractional crystallization to comenditic (P.I. > 1.0, Fe/Al* < 1.0) or to pantelleritic (P.I. >1.0, Fe/Al* > 1.0) compositions depends on when iron oxides (magnetite, ilmenite) and Na-Fe silicates (aenigmatite, aegirine-augite, ferrorichterite) crystallize, which is primarily controlled by fO_2, H_2O_m, and fF_2 (Scaillet & Macdonald, 2001, 2003, 2006; Markl *et al.*, 2010; Di Carlo *et al.*, 2010; Marks *et al.*, 2011; Romano *et al.*, 2020.) Oxygen fugacity in particular is widely understood to be a critical variable in controlling the evolution of alkaline igneous rocks in general, with lower values associated with oxide-free assemblages, the crystallization of aegirine-rich pyroxenes, and the driving of residual melts to more strongly peralkaline compositions. The transition from comenditic to pantelleritic compositions is mirrored in intrusive sequences by the transition from miaskitic to agpaitic compositions (Mann *et al.*, 2006; Markl *et al.*, 2010; Marks *et al.*, 2011; Giehl *et al.*, 2013).

Although Pantelleria is the type locality for pantellerite, the pre-Green Tuff eruptive history of the island has been dominated

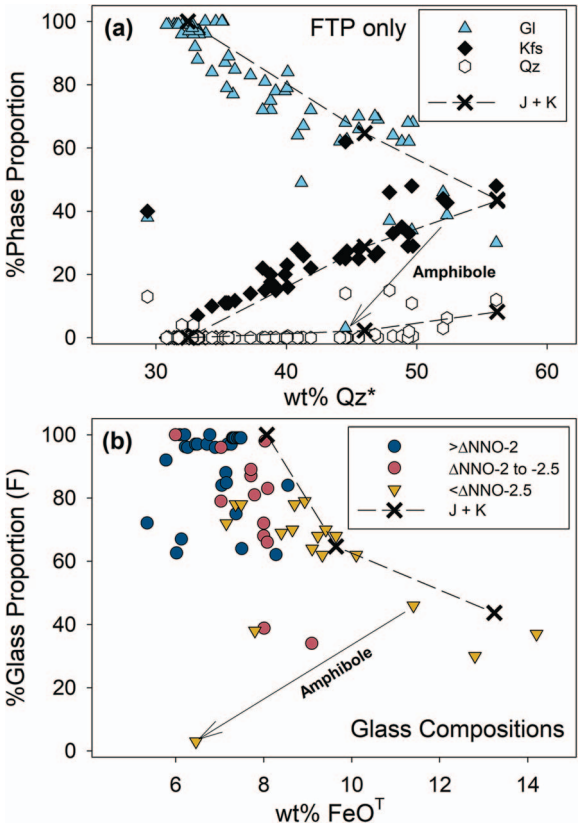

Fig. 15. (a) Percent phase proportions of glass (Gl), alkali feldspar (Kfs), and quartz (Qz) from experiments on FTP (Di Carlo *et al.*, 2010; Romano *et al.*, 2020) plotted versus the Qz* of the glass compositions and with the results of mass balance models J and K from Mida (see Table 11 and Supplementary Table 11). (b) Percent phase proportions of glass only sorted by experimental oxygen fugacity values (relative to NNO) plotted versus wt% FeO^T of the glass and with the results of mass balance models J and K from Mida. 'Amphibole' shows the effect of amphibole crystallization on melt composition under crystal-rich conditions (from 725°C [Run 4–7] to 680°C [Run 9–7] at 150 MPa; Di Carlo *et al.*, 2010).

by eruptions of comenditic trachyte to comenditic ignimbrites, with pantellerites occurring mostly as small inter-caldera volcanic centres, all of which have nearly identical trace-element enrichment patterns and incompatible trace-element ratios that strongly suggest derivation from a common parental magma along broadly similar LLOD (Rotolo *et al.*, 2013, 2021; Jordan *et al.*, 2018, 2021; Romano *et al.*, 2022). The occurrence of both basalt-trachyte-comendite and basalt-trachyte-pantellerite suites in the same volcanic centre has been documented in many peralkaline systems. In some instances, comendite and pantellerite occur as part of the same magma series, with the latter interpreted as the result of continued fractional crystallization of the former; in these series, pantellerite eruptive products are subordinate in volume to the comendites and are, relative to other pantellerites, only mildly peralkaline (P.I. ≤ 1.3). Examples of these include Torfajökull, Iceland (McGarvie *et al.*, 2006), Olkaria, Kenya (Macdonald *et al.*, 2008b; Marshall *et al.*, 2009), and numerous volcanic centres in the Basin and Range Province, USA (Wallace *et al.*, 1980; Conrad, 1984; Mathis, 1993; Henry *et al.*, 2017). An exception is the Black Mountain Volcanic Centre in Nevada where a long sequence of comenditic eruptive systems was terminated by a strongly peralkaline ash flow (Macdonald *et al.*, 2019). In other instances, comendite and pantellerite form the end-member of distinct magma series. In addition to Pantelleria, these include Boseti, Ethiopia (Ronga *et al.*, 2009), Nemrut, Turkey (Macdonald *et al.*, 2015), Changbaishan, China-North Korea (Andreeva *et al.*, 2019), and Terceira, Azores (Mungall & Martin, 1995, 1996).

On Pantelleria, ilmenite is the dominant oxide phase in pantellerites whereas ulvöspinel-rich magnetite is the dominant phase in comendites (Jordan, 2014; Jordan *et al.*, 2021). Mungall & Martin (1995) observed the same for the comenditic Santa Barbara and pantelleritic Pico Alto volcanic suites at Terceira, Azores, which they attributed to differences in oxygen fugacity (higher for trachyte-comendite and lower for trachyte-pantellerite) that they postulated were the result of early degassing of water and H_2 from Santa Barbara trachytes. A salient feature of the Pico Alto pantellerites reported by Mungall & Martin (1996) are matrix glasses and melt inclusions with extreme compositions of up to 13.3 wt% FeO^T, 3600 ppm Zr, and P.I. ≈ 4.3, which they also ascribed to very low oxygen fugacity and described as geochemically analogous to the hypersolvus (miaskitic) phase of the rare-metal rich Strange Lake granite in Québec-Labrador, Canada (Siegel *et al.*, 2018).

The relative oxygen fugacity of silicic magmas typically overlaps with, and is inherited from, the parental mafic magmas (Carmichael, 1991). Major and trace element data strongly suggest that the four suites discussed in this study were derived from a similar parent along similar differentiation paths from transitional basalt to trachyte and through a 'thermal valley' dominated by the fractionation of alkali feldspar to pantelleritic compositions that plot near a 'whole-rock minimum' in a Q-Or-Ab-Ac-Ns projection. Compositional differences between the suites can be attributed to variability in the fractionating mafic phases, which is mainly controlled by the oxygen fugacity during crystallization.

Although pressure has negligible effect on relative oxygen fugacity, we posit that the differences in oxygen fugacity between the suites—and most markedly between the Green Tuff and Mida suites—are most likely due to differences between the depths of the magma reservoirs and the hydrous nature of these magmas, inherited from their mafic parents. Increases in relative oxygen fugacity with decreasing temperature in pantelleritic systems have been described by Mungall & Martin (1995, 1996) for Terceira and Liszewska *et al.* (2018) for the Green Tuff, who each attributed the change to a reaction between Fe-rich silicate melt and H_2O in the magma *via* thermal dissociation of H_2O. For this mechanism to be viable, the magma must be degassing and H_2 (reduced from H^+ by Fe^{2+} by the reaction $2FeO + H_2O = Fe_2O_3 + H_2$) able to diffuse (Sato, 1978). Diffusion of H_2 in silicate glasses has been experimentally shown to be rapid (Zhang & Ni, 2010) and in order to degas the magma must be saturated in a fluid phase. Water saturation in pantelleritic melts is primarily a function of pressure (Romano *et al.*, 2021), with lower temperatures and higher sodium contents also contributing to increased solubility (Stabile *et al.*, 2018; Allabar *et al.*, 2022). We therefore suggest that although all these pantelleritic suites were sourced from a similar mafic parent along similar liquid lines of descent, differences in the evolutionary paths beyond the 'minimum' are primarily controlled by the depth of emplacement. Deeper magma reservoirs, such as Mida, had high water contents but remained undersaturated relative to a fluid phase due to higher pressures, which also kept the water dissolved in the melt, oxygen fugacity low, and enabled the crystallization of amphibole. Shallower reservoirs, such as the one that supplied the Green Tuff, had similarly high water contents but became saturated at lower pressures that allowed the water to degas, which ultimately increased the relative oxygen fugacity

and inhibited the crystallization of amphibole. The depth-control will also have important implications for the eruptive potential and style of the system. Furthermore, whether or not the magma degases strongly influences whether soluble rare-metals are retained in the system or lost.

While this discussion is aimed primarily at peralkaline systems, it would be instructive to assess non-peralkaline systems for evidence of a relationship between oxygen fugacity and pressure, for example, the high-Fe rhyolites associated with tholeiitic suites in Iceland.

CONCLUSIONS

- Despite a common basalt-trachyte origin and evolution through a common 'thermal valley', several evolutionary paths exist and there is no unique end point for peralkaline silicic magmas, forming a 'cotectic delta' towards multiple glass minima beyond the whole-rock minimum on the alkali feldspar-quartz cotectic.
- Experiments on both comendites and pantellerite and shown that fractionation at higher fO_2 expands the thermal stability of oxides, which results in residual liquids that are less, or similarly, peralkaline and lower in FeO^T than the bulk compositions, whereas at very low fO_2 (<ΔNNO-2.5) residual liquids have compositions with P.I. up to ~4.3 and up to 14.3 wt% FeO^T (Scaillet & Macdonald, 2003, 2006; Di Carlo *et al.*, 2010; Romano *et al.*, 2020). The close correlation between the compositions of the natural Mida and experimental glasses convincingly demonstrates the validity of this conclusion and suggests that our lower estimate for oxygen fugacity in the Mida system (~ΔNNO-3.0) is accurate.
- A key control is pressure. At high pressures, water stays dissolved in the melt and is available to form amphiboles; at lower pressures, water will exsolve and thermally dissociate resulting in an increase in relative oxygen fugacity. Thus, at higher pressures water will remain dissolved and maintain lower fO_2 in the melt, resulting in a melt that is both water-rich and reduced (cf. Di Carlo *et al.*, 2010), providing ideal conditions for amphibole crystallization. Amphibole formed in the Mida, Altura, and Gadir suites as a result of low temperatures, low fO_2 and high H_2O_m. Its formation was inhibited in the Green Tuff by higher fO_2 and lower H_2O_m.
- Evidence is accumulating on how the depth and nature of the magma reservoirs at Pantelleria have changed over time (Neave, 2020; Jordan *et al.*, 2021; Rotolo *et al.*, 2021). Here we have described a mechanism by which the depth of the reservoir can affect the ultimate fractionation history of the magma.

FUNDING

This work was supported by a University Funded Scholarship grant and a Rowlett Faculty Development Research Award from Eastern Kentucky University to JCW. Financial support from grant number 501-D113–01–01-1130101 for RM, KL, and BB is much appreciated.

DATA AVAILABILITY

The data underlying this article are available in the article and in its online supplementary material.

Supplementary data

Supplementary data are available at *Journal of Petrology* online.

ACKNOWLEDGEMENTS

The authors wish to thank Silvio Rotolo, Marco Brenna, and Anonymous for their thorough reviews and constructive comments, which considerably improved this manuscript. The authors also thank Nina Jordan for the use of her unpublished data and Haley Cabaniss for her help with key figures.

References

Allabar, A., Petri, P. L., Eul, D. & Nowak, M. (2022). An empirical model for peralkaline rhyolitic melts. *Contributions to Mineralogy and Petrology* **177**. https://doi.org/10.1007/s00410-022-01915-8.

Andersen, D. J., Bishop, F. C. & Lindsley, D. H. (1991). Internally consistent solution models for Fe-Mg-Mn-Ti oxides: Fe-Mg-Ti oxides and olivine. *American Mineralogist* **76**, 427–444.

Andersen, D. J., Lindsley, D. H. & Davidson, P. M. (1993). QUILF: a PASCAL program to assess equilibria among Fe-Mg-Mn-Ti oxides, pyroxenes, olivine, and quartz. *Computers & Geosciences* **19**, 1333–1350. https://doi.org/10.1016/0098-3004(93)90033-2.

Andreeva, O. A., Andreeva, I. A. & Yarmolyuk, V. V. (2019). Effect of redox conditions on the evolution of magmas of Changbaishan Tianchi volcano, China-North Korea. *Chemical Geology* **508**, 225–233. https://doi.org/10.1016/j.chemgeo.2018.09.039.

Arzilli, F., Stabile, P., Fabbrizio, A., Landi, P., Scaillet, B., Paris, E. & Carroll, M. R. (2020). Crystallization kinetics of alkali feldspar in peralkaline rhyolitic melts: implications for Pantelleria volcano. *Front Earth Science* **8**, Article 177. https://doi.org/10.3389/feart.2020.00177.

Avanzinelli, R., Bindi, L., Menchetti, S. & Conticelli, S. (2004). Crystallization and genesis of peralkaline magmas from Pantelleria Volcano, Italy: an integrated petrological and crystal-chemical study. *Lithos* **73**, 41–69. https://doi.org/10.1016/j.lithos.2003.10.007.

Bailey, D. K. & Macdonald, R. (1969). Alkali-feldspar fractionation trends and the derivation of peralkaline liquids. *American Journal of Science* **267**, 242–248. https://doi.org/10.2475/ajs.267.2.242.

Bailey, D. K. & Schairer, J. F. (1964). Feldspar-liquid equilibria in peralkaline liquids—the orthoclase effect. *American Journal of Science* **262**, 1198–1206. https://doi.org/10.2475/ajs.262.10.1198.

Bailey, D. K. & Schairer, J. F. (1966). The system Na_2O-Al_2O_3-Fe_2O_3-SiO_2 at 1 atmosphere and the petrogenesis of alkaline rocks. *Journal of Petrology* **7**, 114–170. https://doi.org/10.1093/petrology/7.1.114.

Berman, R. G. (1991). Thermobarometry using multi-equilibrium calculations: a new technique, with petrological applications. *Canadian Mineralogist* **29**, 833–855.

Blundy, J. & Cashman, K. (2008). Petrologic reconstruction of magmatic system variables and processes. *Reviews in Mineralogy & Geochemistry* **69**, 179–239. https://doi.org/10.2138/rmg.2008.69.6.

Brenna, M., Pontesilli, A., Mollo, S., Masotta, M., Cronin, S. J., Smith, I. E. M., Mousfti, M. R. H. & Scarlato, P. (2019). Intra-eruptive trachyte-phonolite transition: natural evidences and experimental constraints on the role of crystal mushes. *American Mineralogist* **104**, 1750–1764. https://doi.org/10.2138/am-2019-6963.

Carmichael, I. S. E. (1962). Pantelleritic liquids and their phenocrysts. *Mineralogical Magazine* **33**, 86–113. https://doi.org/10.1180/minmag.1962.033.257.03.

Carmichael, I. S. E. (1967). The iron-titanium oxides of salic volcanic rocks and their associated ferromagnesian silicates. *Contributions to Mineralogy and Petrology* **14**, 36–64.

Carmichael, I. S. E. (1991). The redox states of basic and silicic magmas: a reflection of their source regions? *Contributions to Mineralogy and Petrology* **106**, 129–141. https://doi.org/10.1007/BF00306429.

Carmichael, I. S. E. & MacKenzie, W. S. (1963). Feldspar-liquid equilibria in pantellerites: an experimental study. *American Journal of Science* **261**, 382–396. https://doi.org/10.2475/ajs.261.4.382.

Carmichael, I. S. E., Nicholls, J. & Smith, A. L. (1970). Silica activity in igneous rocks. *American Mineralogist* **55**, 246–263.

Carmichael, I. S. E., Turner, F. J. & Verhoogen, J. (1974) *Igneous Petrology*. New York: McGraw-Hill.

Catalano, S., De Guidi, G., Lanzafame, G., Monaco, C. & Tortorici, L. (2009). Late Quaternary deformation of the island of Pantelleria: new constraints for the recent tectonic evolution of the Sicily Channel Rift (southern Italy). *Journal of Geodynamics* **48**, 75–82. https://doi.org/10.1016/j.jog.2009.06.005.

Charles, R. W. (1975). The phase equilibria of richterite and ferrorichterite. *American Mineralogist* **60**, 367–374.

Charles, R. W. (1977). The phase equilibria of intermediate compositions on the pseudobinary $Na_2CaMg_5Si_8O_{22}(OH)_2$—$Na_2CaMgFe_5Si_8O_{22}(OH)_2$. *American Journal of Science* **277**, 594–625. https://doi.org/10.2475/ajs.277.5.594.

Civetta, L., Cornette, Y., Crisci, G., Gillot, P. Y., Orsi, G. & Reqeujo, C. S. (1984). Geology, geochronology and chemical evolution of the island of Pantelleria. *Geological Magazine* **121**, 541–562. https://doi.org/10.1017/S0016756800030703.

Civetta, L., Cornette, Y., Gillot, P. Y. & Orsi, G. (1988). The eruptive history of Pantelleria (Sicily Channel) in the last 50 ka. *Bulletin of Volcanology* **50**, 47–57. https://doi.org/10.1007/BF01047508.

Civetta, L., D'Antonio, M., Orsi, G. & Tilton, G. R. (1998). The geochemistry of volcanic rocks from Pantelleria island, Sicily channel: Petrogenesis and characteristics of the mantle source region. *Journal of Petrology* **39**, 1453–1491. https://doi.org/10.1093/petroj/39.8.1453.

Conrad, W. K. (1984). The mineralogy and petrology of compositionally zoned ash flow tuffs, and related silicic volcanic rocks, from the McDermitt caldera complex, Nevada-Oregon. *Journal of Geophysical Research* **89**, 8639–8664. https://doi.org/10.1029/JB089iB10p08639.

Cornette, Y., Crisci, G. M., Gillot, P. Y. & Orsi, G. (1983). Recent volcanic history of Pantelleria: a new interpretation. *Journal of Volcanology and Geothermal Research* **17**, 361–373. https://doi.org/10.1016/0377-0273(83)90076-8.

Della Ventura, G., Iezzi, G., Redhammer, G. J., Hawthorne, F. C., Scaillet, B. & Novembre, D. (2005). Synthesis and crystal-chemistry of alkali amphiboles in the system Na_2O-MgO-FeO-Fe_2O_3-SiO_2-H_2O as a function of f_{O2}. *American Mineralogist* **90**, 1375–1383. https://doi.org/10.2138/am.2005.1682.

Di Carlo, I., Rotolo, S. G., Scaillet, B., Buccheri, V. & Pichavant, M. (2010). Phase equilibrium constraints on pre-eruptive conditions of recent felsic explosive volcanism at Pantelleria Islands, Italy. *Journal of Petrology* **51**, 2245–2276. https://doi.org/10.1093/petrology/egq055.

Ernst, W. G. (1962). Synthesis, stability relations, and occurrence of riebeckite and riebeckite-arfvedsonite solid solutions. *Journal of Geology* **70**, 689–736. https://doi.org/10.1086/626866.

Ferla, P. & Meli, C. (2006). Evidence of magma mixing in the 'Daly Gap' of alkaline suites: a case study from the enclaves of Pantelleria (Italy). *Journal of Petrology* **47**, 1467–1507. https://doi.org/10.1093/petrology/egl015.

Frost, B. R. & Lindsley, D. H. (1992). Equilibria among Fe-Ti oxides, pyroxenes, olivine, and quartz: part II. *Application. American Mineralogist* **77**, 1004–1020.

Frost, B. R., Lindsley, D. H. & Andersen, D. J. (1988). Fe-Ti oxide-silicate equilibria: assemblages with fayalitic olivine. *American Mineralogist* **73**, 727–740.

Gaeta, M. & Mottana, A. (1991). Phase relations of aenigmatite minerals in a syenitic ejectum, Wonchi volcano, Ethiopia. *Mineralogical Magazine* **55**, 529–534. https://doi.org/10.1180/minmag.1991.055.381.05.

Giehl, G., Marks, M. & Nowak, M. (2013). Phase relations and liquid lines of descent of an iron-rich peralkaline phonolitic melt: an experimental study. *Contributions to Mineralogy and Petrology* **165**, 283–304. https://doi.org/10.1007/s00410-012-0809-6.

Giesting, P. A. & Filiberto, J. (2014). Quantitative models linking amphibole composition with magma Cl and OH content. *American Mineralogist* **99**, 852–865. https://doi.org/10.2138/am.2014.4623.

Gioncada, A. & Landi, P. (2010). The pre-eruptive volatile contents of recent basaltic and pantelleritic magmas at Pantelleria (Italy). *Journal of Volcanology and Geothermal Research* **189**, 191–201. https://doi.org/10.1016/j.jvolgeores.2009.11.006.

Grew, E. S., Hålenius, U., Pasero, M. & Barbier, J. (2008). Recommended nomenclature for the sapphirine and surinamite groups (sapphirine supergroup). *Mineralogical Magazine* **72**, 839–876. https://doi.org/10.1180/minmag.2008.072.4.839.

Hawthorne, F. C., Oberti, R., Harlow, G. E., Maresch, W. V., Martin, R. F., Schumacher, J. C. & Welch, M. D. (2012). Nomenclature of the amphibole supergroup. *American Mineralogist* **97**, 2031–2048. https://doi.org/10.2138/am.2012.4276.

Henry, C. D., Castor, S. B., Starkel, W. A., Ellis, B. S., Wolff, J. A., Laravie, J. A., McIntosh, W. C. & Heizler, M. T. Geology and evolution of the McDermitt caldera, northern Nevada and southeastern Oregon, western USA. *Geosphere* **13**, 1066–1112. https://doi.org/10.1130/GES01454.1.

Hodges, F. N. & Barker, D. S. (2017). Solid solution in aenigmatite. *Yearbook Carnegie Institution of Washington* **72**, 578–581.

Jeffery, A. J. & Gertisser, R. (2018). Peralkaline felsic magmatism of the Atlantic islands. *Frontiers in Earth Science* **6**, 145. https://doi.org/10.3389/feart.2018.00145.

Jordan, N. J. (2014) *Pre-Green Tuff explosive eruptive history, petrogenesis and proximal-distal tephra correlations of a peralkaline caldera volcano: Pantelleria, Italy*. Ph.D. thesis,. University of Leicester, Leicester, UK p.275.

Jordan, N. J., Rotolo, S. G., Williams, R., Speranza, F., McIntosh, W. C., Branney, M. J. & Scaillet, S. (2018). Explosive eruptive history of Pantelleria, Italy: repeated caldera collapse and ignimbrite emplacement at a peralkaline volcano. *Journal of Volcanology and Geothermal Research* **349**, 47–73. https://doi.org/10.1016/j.jvolgeores.2017.09.013.

Jordan, N. J., White, J. C., Macdonald, R. & Rotolo, S. G. (2021). Evolution of the magma system of Pantelleria (Italy) from 190 ka to present. *Comptes Rendus Géoscience* **353**, 133–149. https://doi.org/10.5802/crgeos.50.

Kelsey, C. H. (1965). Calculation of the C.I.P.W. norm. *Mineralogical Magazine* **34**, 276–282. https://doi.org/10.1180/minmag.1965.034.268.23.

Kovalenko, V. I., Naumov, V. B., Solovova, I. P., Girnis, A. V., Hervig, R. L. & Boriani, A. (1994). Volatile components, composition, and crystallization conditions of the Pantelleria basalt-pantellerite association magmas, inferred from the melt and fluid inclusion data. *Petrology* **2**, 19–34.

Kunzmann, T. (1999). The aenigmatite-rhönite mineral group. *European Journal of Mineralogy* **11**, 743–756. https://doi.org/10.1127/ejm/11/4/0743.

Lacroix, A. (1930). Les roches hyperalcalines du massif du Fantale et du col de Balla. *Société Géologique de France Mémoire* **14**, 89–102.

Lanzo, G., Landi, P. & Rotolo, S. G. (2013). Volatiles in pantellerite magmas: a case study of the green tuff Plinian eruption (Island of Pantelleria, Italy). *Journal of Volcanology and Geothermal Research* **262**, 153–163. https://doi.org/10.1016/j.jvolgeores.2013.06.011.

Larsen, L. M. (1976). Clinopyroxenes and coexisting mafic minerals from the alkaline Ilímaussaq intrusion, South Greenland. *Journal of Petrology* **17**, 258–290. https://doi.org/10.1093/petrology/17.2.258.

Larsen, L. M. (1977). Aenigmatites from the Ilímaussaq intrusion, South Greenland: chemistry and petrological implications. *Lithos* **10**, 257–270. https://doi.org/10.1016/0024-4937(77)90002-0.

Le Maitre, R. W. (1976). Some problems of the projection of chemical data into mineralogical classifications. *Contributions to Mineralogy and Petrology* **56**, 181–189. https://doi.org/10.1007/BF00399603.

Le Maitre, R.W. (Ed.) (2002). *Igneous Rocks, a Classification and Glossary of Terms: Recommendations of the International Union of Geological Sciences Subcomission on the Systematics of Igneous Rocks*, 2nd Ed. Cambridge University Press, Cambridge, UK, 236 p, https://doi.org/10.1017/CBO9780511535581.

LeMasurier, W., Choi, S. H., Kawachi, Y., Musaka, S. & Rogers, N. (2018). Dual origins for pantellerites, and other puzzles, at Mount Takahe volcano, Marie Byrd Land, West Antarctica. *Lithos* **296-299**, 142–162. https://doi.org/10.1016/j.lithos.2017.10.014.

Lindsley, D. H. (1983). Pyroxene thermometry. *American Mineralogist* **68**, 477–493.

Lindsley, D. H. & Frost, B. R. (1992). Equilibria among Fe-Ti oxides, pyroxene, olivine, and quartz: part I. *Theory. American Mineralogist* **77**, 987–1003.

Liszewska, K. M., White, J. C., Macdonald, R. & Bagiński, B. (2018). Compositional and thermodynamic variability in a stratified magma chamber: evidence from the green tuff ignimbrite (Pantelleria, Italy). *Journal of Petrology* **59**, 2245–2272. https://doi.org/10.1093/petrology/egy095.

Locock, A. J. (2014). An excel spreadsheet to classify chemical analyses of amphiboles following the IMA 2012 recommendations. *Computational Geosciences* **62**, 1–11. https://doi.org/10.1016/j.cageo.2013.09.011.

Lowenstern, J. B. (1994). Chlorine, fluid immiscibility, and degassing in peralkaline magmas from Pantelleria, Italy. *American Mineralogist* **79**, 353–369.

Lowenstern, J. B. & Mahood, G. A. (1991). New data on magmatic H_2O contents of pantellerites, with implications for petrogenesis and eruptive dynamics at Pantelleria. *Bulletin of Volcanology* **54**, 78–83. https://doi.org/10.1007/BF00278208.

Macdonald, R. (1974). Nomenclature and petrochemistry of the peralkaline oversaturated extrusive rocks. *Bulletin of Volcanology* **38**, 498–516. https://doi.org/10.1007/BF02596896.

Macdonald, R., Bagiński, B., Belkin, H. E., Dzierżanowski, P. & Jeżak, L. (2008a). Compositional variations in apatite from a benmoreite - peralkaline rhyolite volcanic suite, Kenya Rift Valley. *Mineralogical Magazine* **72**, 1147–1161. https://doi.org/10.1180/minmag.2008.072.6.1147.

Macdonald, R., Bagiński, B., Belkin, H. E., White, J. C. & Noble, D. C. (2019). The gold flat tuff, Nevada: insights into the evolution of peralkaline silicic magmas. *Lithos* **328-329**, 1–13. https://doi.org/10.1016/j.lithos.2019.01.017.

Macdonald, R., Bagiński, B., Leat, P. T., White, J. C. & Dzierżanowski, P. (2011). Mineral stability in peralkaline silicic rocks: information from trachytes of the Menengai volcano, Kenya. *Lithos* **125**, 553–568. https://doi.org/10.1016/j.lithos.2011.03.011.

Macdonald, R., Bagiński, B., Ronga, F., Dzierżanowski, P., Lustrino, M., Marzoli, A. & Melluso, L. (2012). Evidence for extreme fractionation of peralkaline silicic magmas, the Boseti volcanic complex, Main Ethiopian Rift. *Mineralogy and Petrology* **104**, 163–175. https://doi.org/10.1007/s00710-011-0184-4.

Macdonald, R., Belkin, H. E., Fitton, J. G., Rogers, N. W., Nejbert, K., Tindle, A. G. & Marshall, A. S. (2008b). The roles of fractional crystallization, magma mixing, crystal mush remobilization, and volatile-melt interactions in the genesis of a young basalt-peralkaline rhyolite suite, the greater Olkaria volcanic complex, Kenya rift valley. *Journal of Petrology* **49**, 1515–1547. https://doi.org/10.1093/petrology/egn036.

Macdonald, R., Sumita, M., Schmincke, H.-U., Bagiński, B., White, J. C. & Ilnicki, S. S. (2015). Peralkaline felsic magmatism at the Nemrut volcano, Turkey: impact of volcanism on the evolution of Lake Van (Anatolia) IV. *Contributions to Mineralogy and Petrology* **169**, 34. https://doi.org/10.1007/s00410-015-1127-6.

Macdonald, R., White, J. C. & Belkin, H. E. (2021). Peralkaline silicic extrusive rocks: magma genesis, evolution, plumbing systems and eruption. *Collect C R Geosci* **353**, 7–59. https://doi.org/10.5802/crgeos.97.

Mahood, G. A. (1984). Pyroclastic rocks and calderas associated with strongly peralkaline magmatism. *Journal of Geophysical Research* **89**, 8540–8552. https://doi.org/10.1029/JB089iB10p08540.

Mahood, G. A. & Hildreth, W. (1983). Nested calderas and trapdoor uplift at Pantelleria, strait of Sicily. *Geology* **11**, 722–726. https://doi.org/10.1130/0091-7613(1983)11<722:NCATUA>2.0.CO;2.

Mahood, G. A. & Hildreth, W. (1986). Geology of the peralkaline volcano at Pantelleria, strait of Sicily. *Bulletin of Volcanology* **48**, 143–172. https://doi.org/10.1007/BF01046548.

Mahood, G. A. & Stimac, J. A. (1990). Trace-element partitioning in pantellerites and trachytes. *Geochimica et Cosmochimica Acta* **54**, 2257–2276. https://doi.org/10.1016/0016-7037(90)90050-U.

Mann, U., Marks, M. & Marlk, G. (2006). Influence of oxygen fugacity on mineral compositions in peralkaline melts: the Katzenbuckel volcano, Southwest Germany. *Lithos* **91**, 262–285. https://doi.org/10.1016/j.lithos.2005.09.004.

Markl, G., Marks, M. A. W. & Frost, B. R. (2010). On the controls of oxygen fugacity in the generation and crystallization of peralkaline melts. *Journal of Petrology* **51**, 1831–1847. https://doi.org/10.1093/petrology/egq040.

Marks, M. A. W., Hettmann, K., Schilling, J., Frost, B. R. & Markl, G. (2011). The mineralogical diversity of alkaline igneous rocks: critical factors for the transition from miskitic to agpaitic phase assemblages. *Journal of Petrology* **52**, 439–455. https://doi.org/10.1093/petrology/egq086.

Marshall, A. S., Macdonald, R., Rogers, N. W., Fitton, J. G., Tindle, A. G., Nejbert, K. & Hinton, R. W. (2009). Fractionation of peralkaline silicic magmas: the Greater Olkaria Volcanic Complex, Kenya Rift Valley. *Journal of Petrology* **50**, 323–359. https://doi.org/10.1093/petrology/egp001.

Mathis, A. C. (1993) *Geology and petrology of a 26-Ma trachybasalt to peralkaline rhyolite suite exposed at Hart Mountain, southern Oregon*. MS thesis, Oregon State University, Corvallis, Oregon, USA, p.141.

McDonough, W. F. & Sun, S. S. (1995). The composition of the Earth. *Chemical Geology* **120**, 223–253. https://doi.org/10.1016/0009-2541(94)00140-4.

McGarvie, D. W., Burgess, R., Tindle, A. G., Tuffen, H. & Stevenson, J. A. (2006). Pleistocene rhyolitic volcanism at Torfajökull, Iceland: eruption ages, glaciovolcanism, and geochemical evolution. *Jökull* **56**, 57–75.

Métrich, N. & Rutherford, M. J. (1992). Experimental study of chlorine behavior in hydrous silicic melts. *Geochimica et Cosmochimica Acta* **56**, 607–616. https://doi.org/10.1016/0016-7037(92)90085-W.

Métrich, N., Susini, J., Foy, E., Farges, F., Massare, D., Sylla, L., Lequien, S. & Bonnin-Mosbah, M. (2006). Redox state of iron in peralkaline rhyolitic glass/melt: X-ray absorption micro-spectroscopy experiments at high temperature. *Chemical Geology* **231**, 350–363. https://doi.org/10.1016/j.chemgeo.2006.02.001.

Morimoto, N. (1989). Nomenclature of pyroxenes. *Canadian Mineralogist* **27**, 143–156.

Mungall, J. E. & Martin, R. F. (1995). Petrogenesis of basalt-comendite and basalt-pantellerite suites, Terceira, Azores, and some implications for the origin of ocean-island rhyolites. *Contributions to Mineralogy and Petrology* **119**, 43–55. https://doi.org/10.1007/BF00310716.

Mungall, J. E. & Martin, R. F. (1996). Extreme differentiation of peralkaline rhyolite, Terciera, Azores: a modern analogue of strange Lake, Labrador? *The Canadian Mineralogist* **34**, 769–777.

Neave, D. A. (2020). Chemical variability in peralkaline magmas and magma reservoirs: insights from the Khaggiar lava flow, Pantelleria, Italy. *Contributions to Mineralogy and Petrology* **175**, 1–21. https://doi.org/10.1007/s00410-020-01678-0.

Neave, D. A., Fabbro, G., Herd, R. A., Petrone, C. M. & Edmonds, M. (2012). Melting, differentiation and degassing at the Pantelleria volcano, Italy. *Journal of Petrology* **53**, 637–663. https://doi.org/10.1093/petrology/egr074.

Nekvasil, H. & Burnahm, C. W. (1987) The calcluated individual effects of pressure and water content on phase equilibria in the granite system. In: Mysen B. O. (ed) *Magmatic processes: physiochemical principles*. Geochemical Society, Special Publication, **1** pp. 433–445. University Park, Pennsylvania, USA.

Nicholls, J. & Carmichael, I. S. E. (1969). Peralkaline acid liquids: a petrological study. *Contributions to Mineralogy and Petrology* **20**, 268–294. https://doi.org/10.1007/BF00377480.

Nicholls, J., Carmichael, I. S. E. & Stormer, J. C., Jr. (1971). Silica activity and P_{total} in igneous rocks. *Contributions to Mineralogy and Petrology* **33**, 1–20. https://doi.org/10.1007/BF00373791.

O'Neil, H. S. C. & Pownceby, M. I. (1993). Thermodynamic data from redox reactions at high temperatures. I. an experimental and theoretical assessment of the electrochemical method using stabilized zirconia electrolytes, with revised values for the Fe-"FeO", Co-CoO, Ni-NiO, and Cu-Cu2O oxygen buffers, and new data for the W-WO_2 buffer. *Contributions to Mineralogy and Petrology* **114**, 296–314.

Orsi, G., Ruvo, L. & Scarpati, C. (1989). The Serra della Fastuca tephra at Pantelleria: physical parameters for an explosive eruption of peralkaline magma. *Journal of Volcanology and Geothermal Research* **39**, 55–60. https://doi.org/10.1016/0377-0273(89)90020-6.

Papike JJ, Cameron KL & Baldwin K (1974). Amphiboles and pyroxenes: characterization of Other than quadrilateral components and estimates of ferric iron from microprobe data. *Geological Society of America Abstracts with Programs* **6**, 1053–1054.

Parker, D. F. & White, J. C. (2008). Large-scale silicic alkalic magmatism associated with the buckhorn caldera, Trans-Pecos Texas, USA: comparison with Pantelleria, Italy. *Bulletin of Volcanology* **70**, 403–415. https://doi.org/10.1007/s00445-007-0145-2.

Pasero, M., Kampf, A. R., Ferraris, C., Pekov, I. V., Rakovan, J. & White, T. J. (2010). Nomenclature of the apatite supergroup minerals. *European Journal of Mineralogy* **22**, 163–179. https://doi.org/10.1127/0935-1221/2010/0022-2022.

Pouchou, J.L. & Pichoir, J.F. (1991). Quantitative analysis of homogeneous or stratified microvolumes applying the model 'PAP'. In: Heinrich, K.F.J. & Newbury, D.E. (eds) *Electron Probe Quantitation*. Plenum Press, New York, 31–75, https://doi.org/10.1007/978-1-4899-2617-3_4.

Pownceby, M. I. & O'Neil, H. S. C. (1994). Thermodynamic data from redox reactions at high temperatures III. Activity-composition relations in Ni-Pd alloys from EMF measurements at 850-1250 K, and calibration of the NiO + Ni-Pd assemblage as a redox sensor. *Contributions to Mineralogy and Petrology* **116**, 327–339. https://doi.org/10.1007/BF00306501.

Prosperini, N., Perugini, D., Poli, G. & Manetti, P. (2000). Magmatic enclaves distribution within the Khaggiar lava dome (Pantelleria, Italy): implication for magma chamber dynamics and eruption. *Acta Vulcanologica* **12**, 37–47.

Ren, M., Omenda, P. A., Anthony, E. Y., White, J. C., Macdonald, R. & Bailey, D. K. (2006). Application of the QUILF thermobarometer to the peralkaline trachytes and pantellerites of the Eburru volcanic complex, East African rift, Kenya. *Lithos* **91**, 109–124. https://doi.org/10.1016/j.lithos.2006.03.011.

Romano, P., Andújar, J., Scaillet, B., Romengo, N., Di Carlo, I. & Rotolo, S. G. (2018). Phase equilibria of Pantelleria trachytes (Italy): constraints on pre-eruptive conditions and on the metaluminous to peralkaline transition in silicic magmas. *Journal of Petrology* **59**, 559–588. https://doi.org/10.1093/petrology/egy037.

Romano, P., Di Carlo, I., Andújar, J. & Rotolo, S. G. (2021). Water solubility in trachytic and pantelleritc melts: an experimental study. *Collect C R Geosci* **353**, 315–331. https://doi.org/10.5802/crgeos.75.

Romano, P., Scaillet, B., White, J. C., Andújar, J., Di Carlo, I. & Rotolo, S. G. (2020). Experimental and thermodynamic constraints on mineral equilibrium in pantelleritic magmas. *Lithos* **376-377**, 105793. https://doi.org/10.1016/j.lithos.2020.105793.

Romano, P., White, J. C., Ciulla, A., Di Carlo, I., D'Oriano, C., Landi, P. & Rotolo, S. G. (2019). Volatile and trace element contents in melt inclusions from the zoned green tuff ignimbrite (Pantelleria): petrological inferences. *Annals of Geophysics* **61**. https://doi.org/10.4401/ag-7671.

Romano, P., White, J. C., Rotolo, S. G., Jordan, N. J., Cirrincione, R., De Giorgio, G., Fiannacca, P. & Vaccaro, E. (2022). Contrasting styles of inter-caldera volcanism in a peralkaline system: case studies from Pantelleria (Sicily Channel, Italy). *Minerals* **12**, 406. https://doi.org/10.3390/min12040406.

Ronga, F., Lustrino, M., Marzoli, A. & Melluso, L. (2010). Petrogenesis of a basalt-comendite-pantellerite rock sutie: the Boseti volcanic complex (main Ethiopian rift). *Mineralogy and Petrology* **98**, 227–243. https://doi.org/10.1007/s00710-009-0064-3.

Rotolo, S. G., La Felice, S., Mangalaviti, A. & Landi, P. (2007). Geology and petrochemistry of the recent (<25 ka) silicic volcanism at Pantelleria Island. *Bollettino della Societá Geologica Italiana* **126**, 191–208.

Rotolo, S. G., Scaillet, S., Speranza, F., White, J. C., Williams, R. & Jordan, N. J. (2021). Volcanological evolution of Pantelleria Island (Strait of Sicily) peralkaline volcano: a review. *Comptes Rendus Géoscience* **353**, 111–132. https://doi.org/10.5802/crgeos.51.

Rotolo, S. G., Scaillet, S. G., La Felice, S. & Vita-Scaillet, G. (2013). A revision of the structure and stratigraphy of pre-green tuff ignimbrites at Pantelleria (Strait of Sicily). *Journal of Volcanology and Geothermal Research* **250**, 61–74. https://doi.org/10.1016/j.jvolgeores.2012.10.009.

Roux, J. & Varet, J. (1975). Alkali feldspar liquid equilibrium relationships in peralkaline oversaturated systems and volcanic rocks. *Contributions to Mineralogy and Petrology* **49**, 67–81. https://doi.org/10.1007/BF00371080.

Salters, V. J. M. & Stracke, A. (2004). Composition of depleted mantle. *Geochemistry Geophysics Geosystems* **5**(5), Q05004. https://doi.org/10.1029/2003GC000597.

Sato, M. (1978). Oxygen fugacity of basaltic magmas and the role of gas-forming elements. *Geophysical Research Letters* **5**, 447–449. https://doi.org/10.1029/GL005i006p00447.

Scaillet, B., Holtz, F. & Pichavant, M. (2016). Experimental constraints on the formation of silicic magmas. *Elements* **12**, 109–114. https://doi.org/10.2113/gselements.12.2.109.

Scaillet, B. & Macdonald, R. (2001). Phase relations of peralkaline silicic magmas and petrogeneic implications. *Journal of Petrology* **42**, 825–845. https://doi.org/10.1093/petrology/42.4.825.

Scaillet, B. & Macdonald, R. (2003). Experimental constraints on the relationships between peralkaline rhyolites of the Kenya rift valley. *Journal of Petrology* **44**, 1867–1894. https://doi.org/10.1093/petrology/egg062.

Scaillet, B. & Macdonald, R. (2006). Experimental constraints on pre-eruption conditions of pantelleritic magmas: evidence from the Eburru complex, Kenya rift. *Lithos* **91**, 95–108. https://doi.org/10.1016/j.lithos.2006.03.010.

Scaillet, S., Rotolo, S. G., La Felice, S. & Vita-Scaillet, G. (2011). High-resolution $^{40}Ar/^{39}Ar$ chronostratigraphy of the post-caldera (<20 ka) volcanic activity at Pantelleria, Sicily Strait. *Earth and Planetary Science Letters* **309**, 280–290. https://doi.org/10.1016/j.epsl.2011.07.009.

Scaillet, S., Vita-Scaillet, G. & Rotolo, S. G. (2013). Millennial-scale phase relationships between ice-core and Mediterranean marine records: insights from high-precision $^{40}Ar/^{39}Ar$ dating of the green tuff of Pantelleria, Sicily Strait. *Quaternary Science Reviews* **78**, 141–154. https://doi.org/10.1016/j.quascirev.2013.08.008.

Siegel, K., Vasyukova, O. V. & Williams-Jones, A. E. (2018). Magmatic evolution and controls on rare metal-enrichment of the Strange Lake A-type peralkaline granitic pluton, Québec-Labrador. *Lithos* **308-309**, 34–52. https://doi.org/10.1016/j.lithos.2018.03.003.

Signorelli, S. & Carroll, M. R. (2002). Experimental study of Cl solubility in hydrous alkaline melts: constraints on the theoretical maximum amount of Cl in trachytic and phonolitic melts. *Contribution to Mineralogy and Petrology* **143**, 209–218.

Speranza, F., Landi, P., Caracciolo, F. D. & Pignatelli, A. (2010). Paleomagnetic dating of the most recent silicic eruptive activity at Pantelleria (Strait of Sicily). *Bulletin of Volcanology* **72**, 847–858. https://doi.org/10.1007/s00445-010-0368-5.

Stabile, P., Arzilli, F. & Carroll, M. R. (2021). Crystallization of peralkaline rhyolitic magmas: pre- and syn-eruptive conditions of the Pantelleria system. *Collect C R Geosci* **353**, 151–170. https://doi.org/10.5802/crgeos.72.

Stabile, P., Radica, F., Bello, M., Behrens, H., Carroll, M. R., Paris, E. & Giuli, G. (2018). H_2O solubility in pantelleritic melts: pressure and alkali effects. *Neues Jahrbuch für Mineralogie* **195**, 1–9. https://doi.org/10.1127/njma/2017/0060.

Thompson, R. N. & MacKenzie, W. S. (1967). Feldspar-liquid equilibria in peralkaline acid liquids: an experimental study. *American Journal of Science* **265**, 714–734. https://doi.org/10.2475/ajs.265.8.714.

Tuttle, O. F. & Bowen, N. L. (1958). Origin of granite in the light of experimental studies in the system NaAlSi3O8-KAlSi3O8-SiO2-H2O. *Geological Society of America Memoir* **74**, 153. https://doi.org/10.1130/MEM74-p1.

Wallace, A. B., Drexler, J. W., Grant, N. K. & Noble, D. C. (1980). Icelandite and aenigmatite-bearing pantellerite from the McDermitt caldera complex, Nevada-Oregon. *Geology* **8**, 380–384. https://doi.org/10.1130/0091-7613(1980)8<380:IAAPFT>2.0.CO;2.

Webster, J. D., Iverson, A. A., Rowe, M. C. & Webster, P. M. (2020). Chlorine and felsic magma evolution: modelling the behavior of an under-appreciated volatile component. *Geochimica et Cosmochimica Acta* **271**, 248–288. https://doi.org/10.1016/j.gca.2019.12.002.

Webster, J. D., Vetere, F., Botcharnikov, R. E., Golfdoff, B., McBirney, A. & Doherty, A. L. (2015). Experimental and modeled chlorine solubilities in aluminosilicate melts at 1 to 7000 bars and 700 to 1250°C: applications to magmas of Augustine volcano, Alaska. *American Mineralogist* **100**, 522–535. https://doi.org/10.2138/am-2015-5014.

Wen, S. & Nekvasil, H. (1994). SOLVCALC: an interactive graphics program package for calculating the ternary feldspar solvus and for two-feldspar geothermometry. *Computers & Geosciences* **20**, 1025–1040. https://doi.org/10.1016/0098-3004(94)90039-6.

White, J. C. (2011). A method for estimating temperature and oxygen fugacity for an assemblage of clinopyroxene, aenigmatite, ilmenite, and quartz in peraklalic rhyolite. *Geological Society of America Abstracts with Programs* **43**(5), 90.

White, J. C., Miggins, D. M. & Macdonald, R. (2022). New $^{40}Ar/^{39}Ar$ ages for the Montagna Grande-Monte Gibele trachyte shield volcano, Pantelleria (Strait of Sicily Rift Zone), Italy. *Geological Society of America Abstracts with Programs* **54**(5), 119650. https://doi.org/10.1130/abs/2022AM-381805.

White, J. C., Neave, D. A., Rotolo, S. G. & Parker, D. F. (2020). Geochemical constraints on mantle sources and basalt petrogenesis in the Strait of Sicily Rift (Italy): insights into the importance of short lengthscale mantle heterogeneity. *Chemical Geology* **545**, 119650. https://doi.org/10.1016/j.chemgeo.2020.119650.

White, J. C., Parker, D. F. & Ren, M. (2009). The origin of trachyte and pantellerite from Pantelleria, Italy: insights from major element, trace element, and thermodynamic modelling. *Journal of Volcanology and Geothermal Research* **179**, 33–55. https://doi.org/10.1016/j.jvolgeores.2008.10.007.

White, J. C., Ren, M. & Parker, D. F. (2005). Variation in mineralogy, temperature, and oxygen fugacity in a suite of strongly peralkaline lavas and tuffs, Pantelleria, Italy. *The Canadian Mineralogist* **43**, 1331–1347. https://doi.org/10.2113/gscanmin.43.4.1331.

Wilke, S., Holtz, F., Neave, D. A. & Almeev, R. (2017). The effect of anorthite content and water on quartz-feldspar cotectic compositions in the rhyolitic system and implications for geobarometry. *Journal of Petrology* **58**, 789–818. https://doi.org/10.1093/petrology/egx034.

Williams, R. (2010) *Emplacement of radial pyroclastic density currents over irregular topography: the chemically zoned, low aspect-ratio Green Tuff ignimbrite*. PhD thesis,. University of Leicester, Leicester, UK, p.232.

Williams, R., Branney, M. J. & Barry, T. L. (2014). Temporal and spatial evolution of a waxing then waning catastrophic density current revealed by chemical mapping. *Geology* **42**, 107–110. https://doi.org/10.1130/G34830.1.

Zhang, Y. & Ni, H. (2010). Diffusion of H, C, and O components in silicate melts. *Reviews in Mineralogy & Geochemistry* **72**, 171–225. https://doi.org/10.2138/rmg.2010.72.5.